

# Are long-period body wave coda caused by lateral heterogeneity?

Filip Neele and Roel Snieder

Department of Theoretical Geophysics, University of Utrecht, PO Box 80.021, 3508 TA Utrecht, The Netherlands

Accepted 1991 May 8. Received 1991 March 11; in original form 1990 September 12

## SUMMARY

Data from two broad-band arrays in western Europe (NARS and GRF) are used to study the character of long-period body wave coda. The events studied are at epicentral distances of  $40^\circ$  to  $60^\circ$ , in the Hindu Kush region and on the Mid-Atlantic Ridge, sampling the upper mantle to a depth of about 1000 km. The periods studied are 5–50 s. The long-period coda of  $P$  at GRF (interstation distance about 10 km) are strongly coherent, whereas the long-period coda of  $PP$ -,  $PPP$ - and  $S$ -waves are incoherent. This indicates that the latter coda consists of scattered waves. To investigate the nature of the scattering process, the data of GRF are analysed for slowness and azimuth variations in the coda intervals. A new beamforming algorithm is presented to deal with the low frequencies and relatively short time intervals. The method is based on Backus–Gilbert inverse theory. The results show that the incoherent long-period coda intervals almost entirely consist of surface waves; these waves are scattered from the preceding body waves. Some calculations with linearized theory for body wave to Rayleigh wave conversion at topography at the surface or at the Moho show that realistic scatterers can account for the observed (constant) coda level. The beamforming results show that the phases in the  $P$  coda all arrive along the great circle. As scattering calculations point out that body wave to body wave scattering is inefficient, it is concluded that the long-period  $P$  coda does not contain a significant amount of scattered energy. Synthetic seismograms obtained with the reflectivity method show that spherically symmetric upper mantle models can explain these coda waves. For events in the Hindu Kush region, an upper mantle with a thick lid overlying a pronounced low-velocity zone (LVZ) is necessary to explain the character of the  $P$  coda at GRF. Such an upper mantle agrees with previous studies of similar great circle paths. The strong coherence of the  $P$  coda at GRF is lost on the scale of NARS (station separation about 200 km). This suggests lateral variations in the upper mantle at a scale of about 200 km. It appears from previous studies of the upper mantle under Europe that these variations must be sought in the LVZ. It is shown that the long-period  $P$  coda is sensitive to variations in the  $P$  velocity structure of the LVZ. This suggests the  $P$  coda (i.e.  $PdP$  phases) as a tool for monitoring lateral variations in the LVZ and possibly to prove the existence or absence of a LVZ in the  $P$  velocity.

**Key words:** body wave coda, GRF, NARS, scattering, upper mantle.

## INTRODUCTION

In this study the long-period body wave coda are used to infer which wave propagation phenomena are responsible for different parts of the seismogram. The central problem is to find out what class of Earth models is consistent with the data and whether different parts of the seismogram require different classes of models (spherically symmetric versus laterally heterogeneous) and different types of theory. The

aim is not to find models that exactly fit the data, but rather to find constraints on the class of possible models.

The body wave coda have received much attention in the literature. Both laterally heterogeneous and homogeneous upper mantle models have been used to explain the body wave coda. In a spherically symmetric model, top-side reverberations on the upper mantle discontinuities, either single or multiple, cause coda waves, such as the leaky, long-period  $PL$  mode (Oliver & Major 1960; Helmberger &

Engen 1980; Baag & Langston 1985) or single reverberations observed in short-period  $P$  coda (e.g., Husebye & Madariaga 1970; Gutowski & Kanasevich 1974); bottom-side reflections produce precursors to  $PP$  (Bolt 1970; Wajeman 1988; Shearer 1990) or  $P'P'$  (Whitcomb & Anderson 1970; Husebye, Haddon & King 1977; Nakanishi 1988; Davis, Kind & Sacks 1989). Waves may also be converted at upper mantle discontinuities (e.g., Barley, Hudson & Douglas 1982; Paulssen 1985, 1988b; Kind & Vinnik 1988). The scattering approach has been very successful in explaining short-period coda waves. Coda waves have been interpreted as waves scattered either singly or multiply in a medium with random velocity fluctuations. Many studies have been devoted to the determination of statistical parameters describing the random medium (e.g., Aki 1973; Kennett 1987; Flatté & Wu 1988; Korn 1988). Interpreting coda waves from local events as backscattered waves may yield estimates of the scalelengths present (Aki & Chouet 1975; Gao *et al.* 1983; Sato 1984). Lateral heterogeneity in an otherwise plane layered or homogeneous medium also produces substantial coda. Levander & Hill (1985) and Hill & Levander (1984) showed that random perturbations in the depth to the interface between a layer and a half-space causes strong coupling between incident body waves and the guided modes of the layer. Lateral variations in layer thickness also produces this coupling (Fuyuki & Matsumoto 1980; Frankel & Clayton 1986; Stead & Helmberger 1988). Greenfield (1971) explained observed short-period  $P$  coda decay by assuming that the coda waves were due to Rayleigh-to- $P$  coupling at topography near the source. Another coda generating mechanism should be mentioned here, namely that of waves reverberating in a plane layered structure. Bouchon (1982) modelled complete seismograms from local events by summing all crustal reverberations. Sereno & Orcutt (1988) explained the coda of  $P_n$  and  $S_n$  as reverberations. When the reflection is specular, a long coda may be built up. In a laterally homogeneous medium such coda waves will be coherent, but if there are variations in the depth to interfaces this coherence will be lost. Palmer *et al.* (1988) show that small lateral variations in, for example, Moho depth results in chaotic behaviour of ray paths of reverberating waves, resulting in completely incoherent coda waves. Bostock & Kennett (1990) computed  $Lg$  ray paths through a laterally varying crustal structure and indeed found that wave paths behave erratically. Toksöz, Dainty & Charrette (1990) studied the influence of random interface depth perturbations (and random velocity perturbations) on the coherency of the short-period  $Lg$  phase. Observed features of the coherency were matched.

Summarizing, it seems that scattering is an efficient mechanism to generate coda waves, especially at short periods. The scattering may occur at random velocity perturbations or at lateral variations of the otherwise plane layered structure, such as depth to the interfaces or tilted interfaces. Coupling between different wave types is expected to occur, especially in the latter case. Repeated specular reflection in a waveguide can also build up considerable coda, and if the waveguide varies laterally this coda will be incoherent. At long periods reverberations in a laterally homogeneous Earth (the  $PL$  mode) offer an

adequate explanation of that part of the coda immediately following the direct  $P$ -wave.

Recently, digital broad-band data have become available from networks in Europe, with a large variety of station separations. These data are used to study coda generation. Epicentral distances range from  $40^\circ$  to about  $60^\circ$ , so essentially the lithosphere and upper mantle structure to a depth of about 1000 km is probed.

A new beamforming algorithm is developed and used to study slowness and azimuth variations throughout the body wave part of the seismogram and to find constraints on possible scattering mechanisms. Slowness and azimuth variations should give some clues as to the nature of the scattering. It is shown that the long-period coda of  $P$  is dominated by energy arriving along the great circle; synthetic seismograms are used to show that laterally homogeneous models of the upper mantle can explain this coda and to put constraints on upper mantle structure. The coda following  $PP/PPP$  and the  $S$ -waves is shown to consist of surface waves, scattered from the preceding body waves at lateral heterogeneity in the lithosphere. (In this context, the term scattering also includes mode conversion; in the process of conversion also the direction of propagation can be different from that of the incident wave.) Finally some calculations using linearized theory are performed to show that realistic scatterers near the surface (such as topography at the surface or the Moho) can explain the observed coda characteristics, such as duration, amplitude and slowness content.

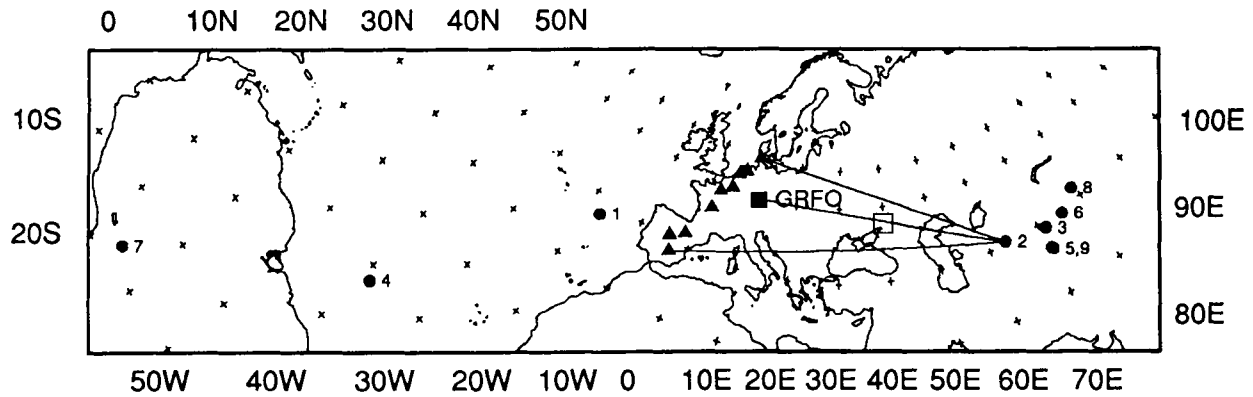
## DATA

Table 1 lists the events used in this study. The event locations are shown in Fig. 1. The data are from the digital, broad-band GRF (Gräfenberg, West Germany) and NARS arrays. We are interested in long-period body waves and consider periods in the range of about 5–50 s.

The GRF array is L-shaped, about 100 km long in the N–S direction, while the E–W extent is about 70 km (Fig. 2). The array consists of 13 broad-band seismometers, of which three have three components. The station separation is typically about 10 km. The NARS array extends from the southernmost part of Sweden to the south of Spain, with an average station separation of 200 km (Fig. 1). This allows a comparison of the characteristics of the wavefield at two scalelengths.

**Table 1.** Event information.

#	Date	Time	Lat	Lon	h	Mb	Dist
1	1983-10-17	19:36:21.6	37.590	-17.410	10	5.9	23.8°
2	1984-03-19	20:28:38.3	40.350	63.360	15	6.4	37.1°
3	1984-10-26	20:22:18.0	39.150	71.350	7	5.9	42.9°
4	1984-11-01	04:48:50.5	8.160	-38.770	10	6.3	58.7°
5	1985-07-29	07:54:44.5	36.210	70.900	102	6.5	44.3°
6	1985-08-23	12:41:56.4	39.490	75.270	40	6.2	45.2°
7	1986-05-09	16:23:48.8	-17.170	-65.620	13	5.6	94.9°
8	1987-01-24	08:09:21.8	41.518	79.293	33	6.0	46.6°
9	1987-05-05	15:40:48.2	36.464	70.683	211	5.7	44.0°



**Figure 1.** The events used in this study (solid circles). Also shown is the position of the Graefenberg array (solid square) and the NARS array, of which a number of stations are plotted (solid triangles). The great circle of event 2 from Table 1 to GRF is plotted, together with the great circles to the outermost NARS stations. The open square represents the bounce point of *PdP* phases to GRF from event 2.

### SPATIAL COHERENCY OF THE SIGNAL

The coherency of the seismic wave field, both as a function of frequency and station separation, contains information on the scalelengths of inhomogeneities in the upper mantle. Many studies have been devoted to the coherency of short-period body waves at seismic arrays (e.g., Aki 1973; King, Haddon & Husebye 1975; Kennett 1987; Korn 1988; Toksöz *et al.* 1989) to obtain information about the structure under the array.

Figure 3 shows a time–distance plot of event 2 recorded by GRF. The traces have been low-passed with corner frequency of 0.15 Hz. The recordings for this event are representative for all events in Table 1. The coherency of the traces up to about 50 s after the *PP*-waves is very clear.

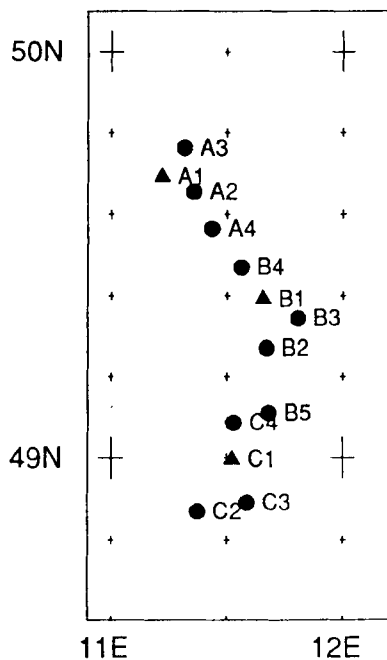


**Figure 2.** The Graefenberg array. Solid circles are one-component stations, solid triangles denote three-component stations.

Almost every waveform can be traced from one station to the next. Note that the noise level is very low, therefore all signal is related to the event and is due to the response of the Earth.

In contrast, the *PP* coda, between the *PP*-waves and the *S*-wave, is clearly dominated by incoherent energy, which is evidence for strong scattering. This sharp contrast is found for all events studied here: a strongly coherent *P* coda, in which nearly all waveforms can be traced from one station to the next, and coda intervals following *PP*- and *S*-waves that are dominated by incoherent energy. At this distance a long-period and large-amplitude *S*-coupled *PL*-wave constitutes the *S* coda, masking incoherent arrivals. Assuming that scattering the lower mantle does not contribute significantly to the wave scattering, the incoherent energy must be caused by scattering somewhere in the upper mantle near the receiving array; scattering near the source will result in coherent energy at this distance and can only be separated from the primary wavefield by detailed slowness and azimuth analysis. This has been done for the short-period *P* coda at 100° by King *et al.* (1975).

Figure 4 shows the data for the same event, recorded by the NARS array. The data are low-passed at 0.15 Hz. The coherency of the *P* coda is no longer present at these station separations, the only coherent arrivals seem to be the main body wave phases. The first part of the *PP* coda that is coherent at GRF is incoherent between NARS stations. This incoherence is not surprising, as the slowness of *PP* [and thus the excitation of *PP*-coupled *PL* (Alsop & Chander 1968) varies across such a large array; furthermore the *PP*-waves are in the triplication zone, causing a rapidly changing *PP*-wavetrain. Note the data from stations NE03 and NE04 at the bottom of Fig. 4; these stations have the same epicentral distance, but they show large differences in the *PP*-wavetrain and to a smaller extent in the *P* coda. Note also stations NE13 and NE14 at the top of Fig. 4: these are close in epicentral distance, but the coda of *P* is incoherent.

The *P* coda of event 4 on GRF records is shown in Fig. 5. The noise level is very low and there is hardly any incoherency in these data. A *PcP* phase arrives at  $t = 650$  s.

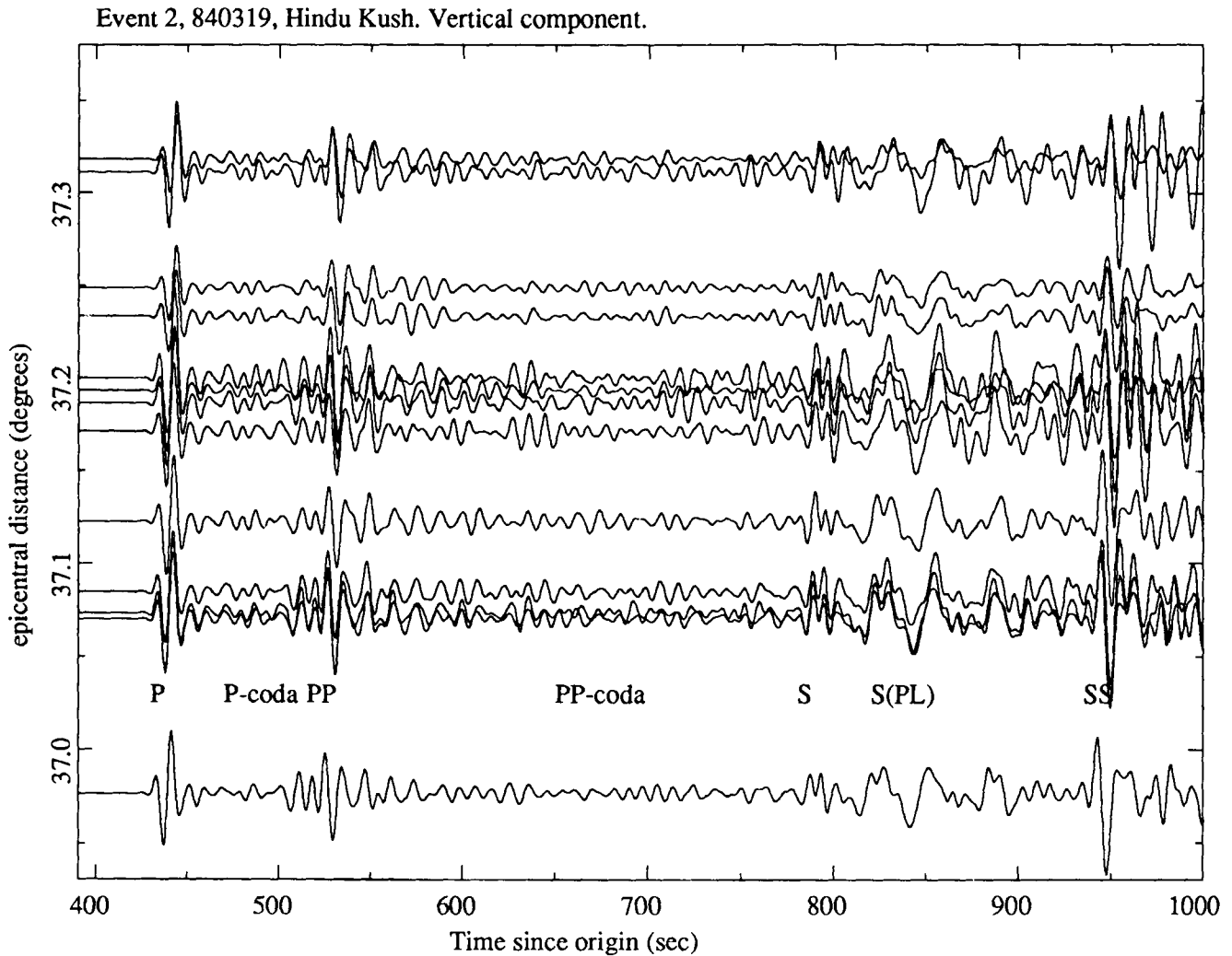


**Figure 3.** Time–distance plot of event 2 recorded by GRF. The arrival time of major phases is indicated. Shown are vertical components, low-passed at 0.15 Hz. Note the strongly coherent *P* coda, and the incoherent coda of *PP*.

### SLOWNESS AND AZIMUTH ANALYSIS

Primary indicators for lateral heterogeneity are the slowness and azimuth of the seismic signal. In a transversely isotropic Earth, any deviations from great circle azimuth must be caused by aspherical structure. An array of stations can be used to measure slowness and azimuth by stacking the individual traces, each delayed or advanced with the proper time shift. This can be done in both time and frequency domain and is known as beamforming. Using this technique, Bungum & Capon (1974) and Levshin & Berteussen (1979) studied surface wave coda recorded at the NORSAR array and found surface waves possibly scattered by continental margins. Capon (1970) used array data of the LASA in Montana and found similarly refracted Rayleigh waves.

A number of beamforming techniques exist in the literature. The simplest algorithm is to simply delay and sum the individual traces: this is conventional beamforming. Its performance can be improved if weights are assigned to each station. Capon (1969) developed a high-resolution algorithm, where the weights are designed such as to optimize the array response. This technique was developed

for application to surface wave problems and is not used in this study; this is due to the inherently short time series in body wave problems, which leads to instability of the high-resolution technique.

For the present study a new beamforming algorithm has been developed for application to body waves. In order to optimize the array response at the long periods used here, a Backus–Gilbert inversion technique (BGI) (Backus & Gilbert 1968) was applied to the conventional (simple weighted phased sum) beamforming. Appendix A gives an outline of the theory. This optimization does not suffer from the drawbacks of the high-resolution technique of Capon (1969), when applied to short intervals. The stacking is done in the frequency domain. Data used are from the GRF array.

Due to the size of GRF only a limited frequency interval can be studied. The frequency-dependent Nyquist slowness for an array with station separation  $D$  is  $p_N = (2Df)^{-1}$ . The slowness interval can be taken such that all physically possible slownesses are included. With the station separation  $D$  of 10 km of GRF and  $0.35 \text{ s km}^{-1}$  ( $2.86 \text{ km s}^{-1}$ ) as an upper limit on expected slownesses [see

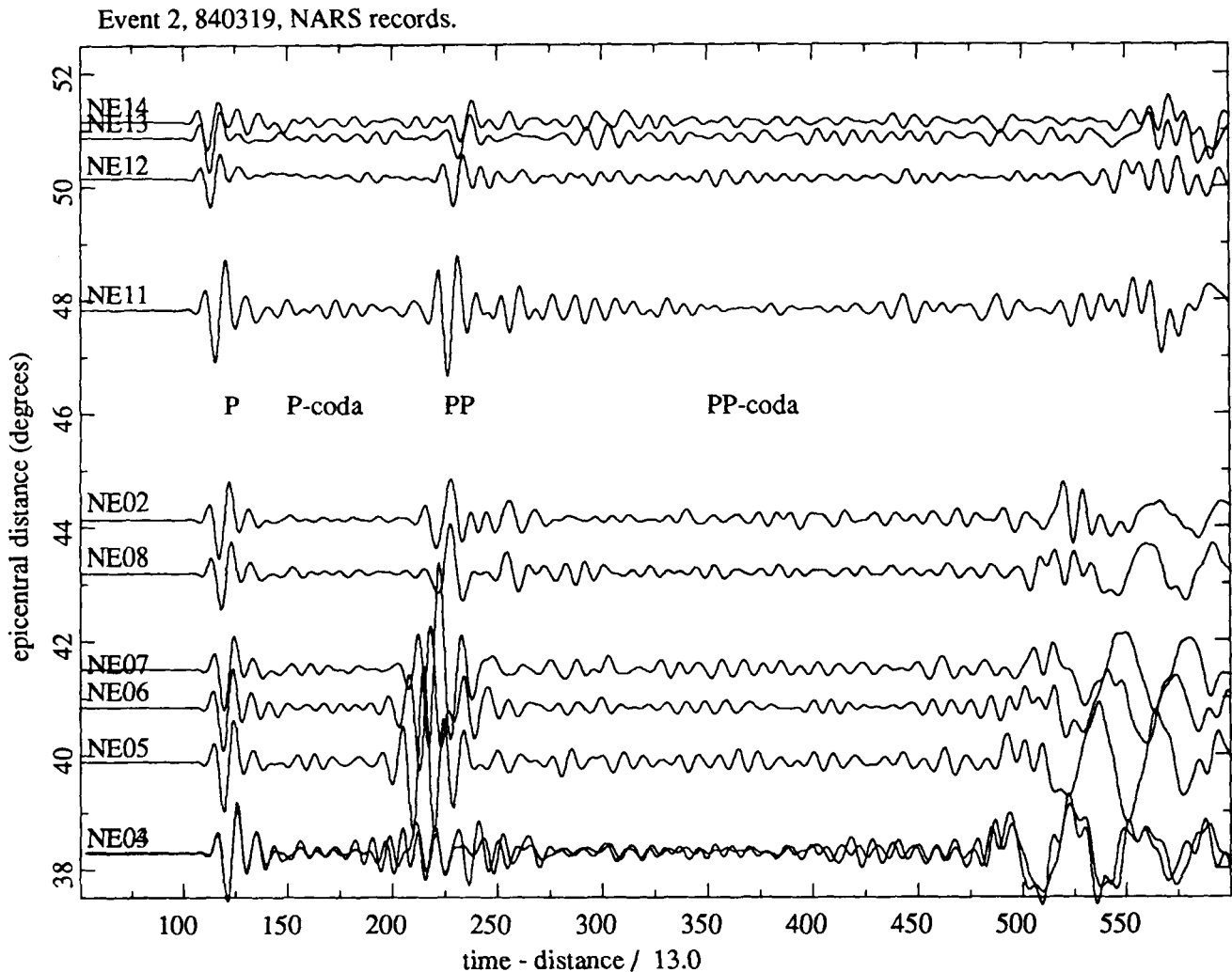


**Figure 4.** Time-distance plot of the event from Fig. 3, now recorded by the NARS array. The data (vertical component) are low-passed at 0.15 Hz. The coherence of the *P* coda that is present in the GRF data is absent at this array.

Dost (1990) for surface wave velocities in western Europe], this gives a frequency of 0.15 Hz below which the Nyquist criterion is satisfied. Frequencies higher than this are spatially aliased and artifacts will contaminate the wavenumber spectrum. A lower bound on the frequency interval is obtained by considering that waves with wavelengths greater than the extent of the array are not resolved very well. Thus, 0.03 Hz is a safe lower bound. The BGI is applied only to slownesses  $|p| < 0.35 \text{ s km}^{-1}$ .

The events in Table 1 were chosen to have a backazimuth near either  $80^\circ$  or  $260^\circ$ . In this way one has the best azimuthal resolution in the direction of the source, so that one best recognize any deviations from great circle azimuth. A moving window analysis was applied to the data; the length of the window (100 s) was chosen as a compromise between resolution in the time and frequency domain. The window usually did not overlap. The frequency interval 0.03–0.15 Hz was split into four subintervals. For each subinterval, the traces were prefiltered and Hanning-tapered to avoid artifacts due to the finite window length (see Capon 1970). Then the traces of all stations were Fourier-transformed. Erroneous station calibrations may influence

the results; to prevent this the amplitude spectra were pre-whitened. To remove confusing side lobes from the slowness diagram the CLEAN algorithm (Högbom 1974) was applied.

Figures 6, 7 and 8 show three examples of slowness diagrams, obtained from events 2 and 5. The slowness diagram is plotted in such a way that a wave arriving from the east with slowness  $0.10 \text{ s km}^{-1}$  appears in the plot with  $p_x = 0.10$  and  $p_y = 0 \text{ s km}^{-1}$ . The direction of the great circle is indicated by the solid line. Contour lines are drawn at 2 dB intervals down from the maximum. Fig. 6 shows the slowness diagram for the frequency band 0.10–0.13 Hz for a time interval containing the *P* coda of event 2. The phases in the *P* coda clearly arrive with great circle azimuth. This shows that the coherence of the data in the coda of *P* in Figs 3 and 5 is not due to the long wavelengths in the data (compared to the size of GRF), but to the fact that all energy arrives along the great circle. Fig. 7 is a slowness diagram for a time interval in the coda of *PP*, for the frequency band 0.09–0.12 Hz and the same event. Apart from some energy arriving along the great circle with body wave slowness, there are maxima off the great circle, with a

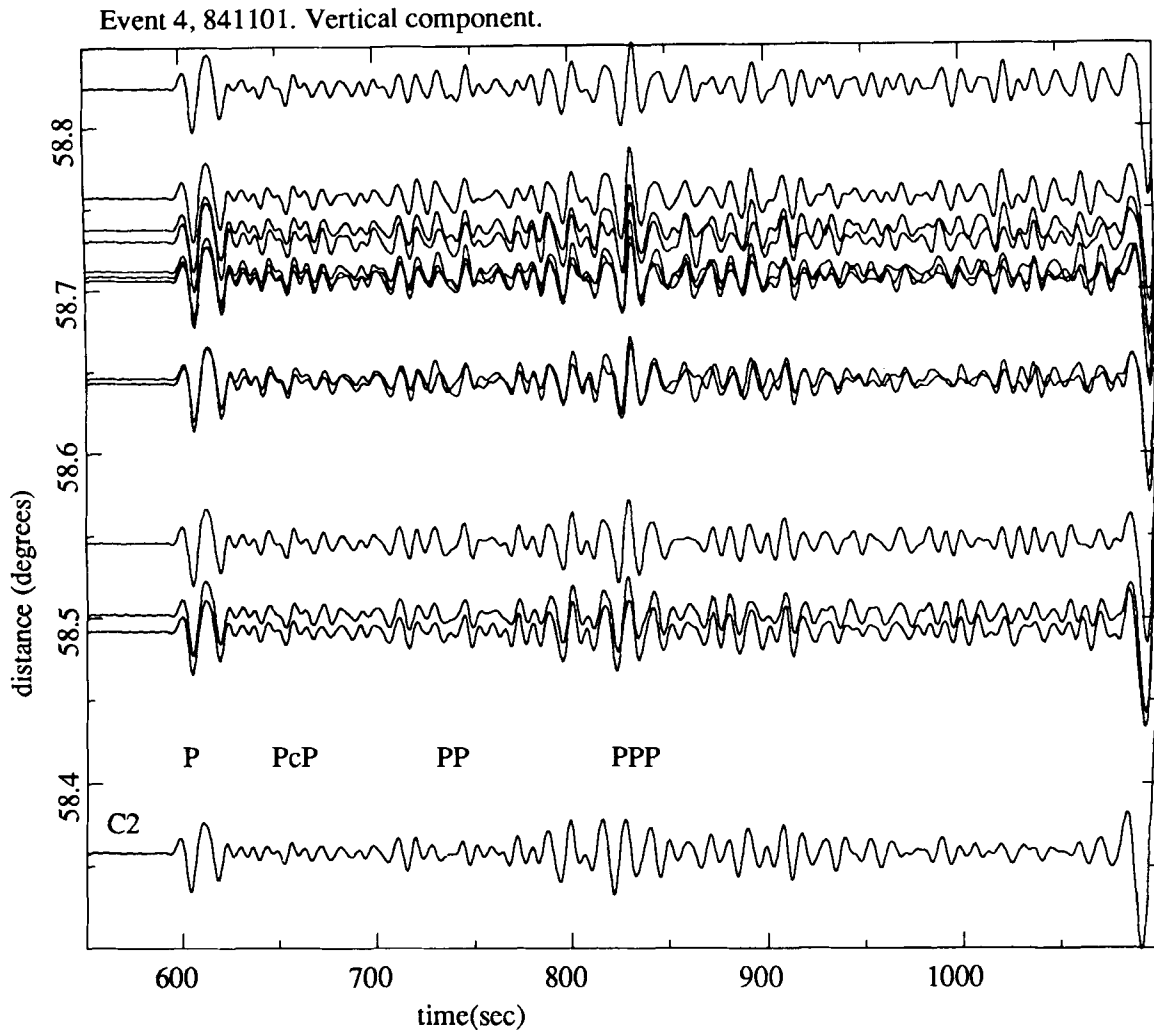


**Figure 5.** Time–distance plot of event 4, recorded by GRF. This event shows a very large coda level. Again the *P* coda is very coherent, whereas the *PP* coda is largely incoherent across the array. The *S*-wave arrives just at the end of the section.

large slowness. These are probably surface waves. As the signal-to-noise ratio for this event is very good, these surface waves must be signal-generated. Fig. 8 is a slowness diagram obtained from the coda of the *S*-wave of event 5. The frequency interval is 0.06–0.08 Hz. There is no energy arriving on the great circle, but there are two surface waves arriving with azimuth deviations of about 25° and 60°.

The results of analysing a large number of slowness diagrams are summarized in three figures. Fig. 9 shows the absolute deviations from great circle azimuth as a function of time, of the most significant energy peaks in the slowness diagrams. The deviations are plotted at the position of the 100 s long, consecutive time intervals in the seismograms. These intervals are labelled with the body wave phase they contain (e.g. *P* or *S*), or with the coda interval they represent (e.g. *PPc1* stands for the first interval in the *PP* coda). The dashed line represents an estimate of the resolution of GRF at a period of 10 s for events with back azimuth of either 80° or 260°. Waves arriving within 10° of the great circle are assumed to arrive on the great circle. Fig. 9 contains data from all frequency bands. The data show a striking increase in deviation from the great circle

after the *PP*-wave. Whereas *P* and *PP* do not show any deviation, the energy in the *PP* coda comes from all directions. A number of short time intervals in the coda of *P* have been analysed as well, but no deviations were found. This is in agreement with the observation that the *P* coda is very coherent and the *PP* coda is not. The large deviations in the *PP* coda persist in the following intervals. Furthermore, the deviations do not seem to increase further into the coda. There seems to be some kind of saturation right in the beginning of the *PP* coda.

Now the wave type of the coda waves has to be established. For this the slowness can be used. The slowness of only the energy peaks off the great circle are plotted in Fig. 10. The energy peaks corresponding to the direct waves are not considered in this plot. Again data from all frequency bands are plotted. The figure shows that apart from some waves with slownesses between 0.1 and 0.2 s km<sup>-1</sup>, most of the scattered waves have a slowness larger than about 0.28 s km<sup>-1</sup>. This corresponds with surface wave slownesses. Therefore, the scattered waves are mainly surface waves and they must have been scattered from body waves to arrive so early in the seismogram.

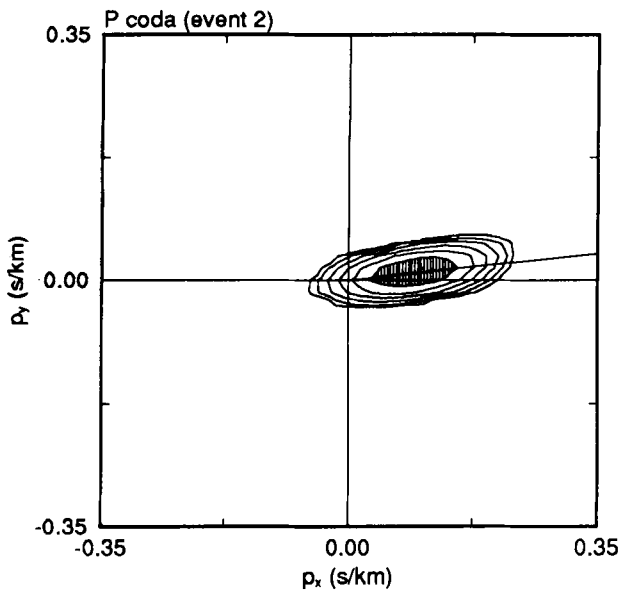


**Figure 6.** Example of a frequency-slowness spectrum. Line contours are in steps of 2 dB down from the maximum. The area above -2 dB is shaded. The spectrum is CLEANed. The spectrum is obtained from event 2,  $450 < t < 510$  s, frequency interval 0.10–0.13 Hz. The interval contains the *P* coda. The back azimuth is indicated by the solid line in the direction of  $84^\circ$ . The phases in the *P* coda arrive on the great circle.

Figure 11 shows the frequency dependence of the direction of incoming of the scattered waves in the coda intervals. The great circle deviation data from all the coda intervals are combined and plotted as a function of frequency. It is clear from the figure that with increasing frequency the deviations from the great circle increase; this means that backward scattering becomes more important at higher frequencies.

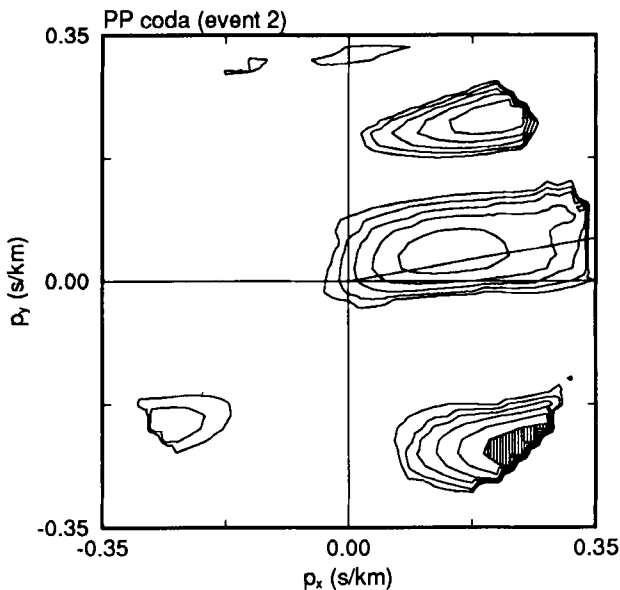


**Figure 7.** As Fig. 2, now for  $600 < t < 700$  s. This spectrum is in the coda of *PP*. Frequency interval 0.09–0.12 Hz. Apart from some energy arriving on the great circle, there are two clear arrivals with slowness about  $0.34 \text{ s km}^{-1}$  and azimuth of  $40^\circ$  and  $131^\circ$ . The slowness of the waves indicates that these are surface waves.

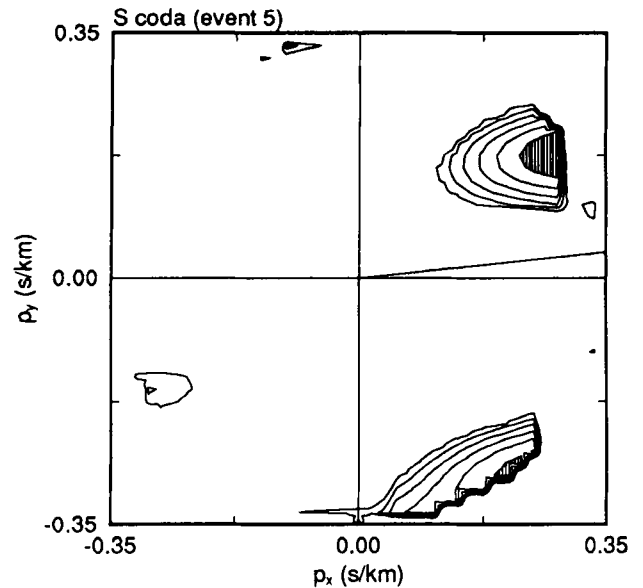


**Figure 8.** As Fig. 2, now for event 5, with  $950 < t < 1050$  s. This interval is in the coda of *S*. Frequency interval 0.06–0.08 Hz. In this case there is no detectable energy arriving on the great circle; surface waves arrive at azimuths of  $58^\circ$  and  $140^\circ$ .

A number of conclusions can be drawn from the analysis of the slowness diagrams, even though the resolution of GRF is not very good. First, the main body wave phases do not show deviations from great circle azimuth, but their coda do. The one exception is the coda of *P*-waves, that shows much less scatter than the coda of *PP*- and *S*-waves. This agrees well with the observation that this coda is very coherent across the array. Secondly, scattering increases with frequency. From scattering theory, this is to be expected, as scattering is a frequency-dependent process, the higher frequencies being scattered more efficiently. Thirdly, the amount of scatter does not increase further in the coda. This suggests a homogeneous coda in both space and time. This is also what is observed in the numerical calculations of Frankel & Wennerberg (1987), for the coda in a medium with random velocity fluctuations. These

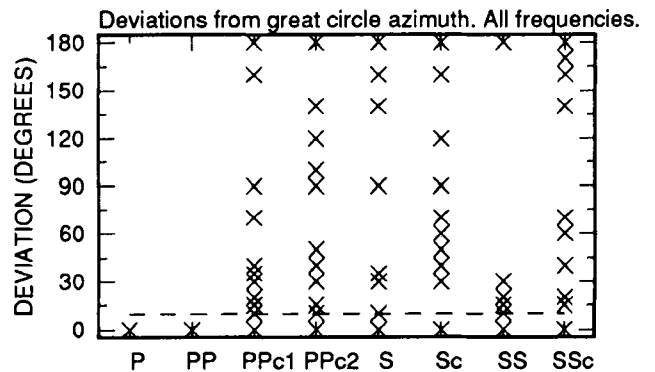


**Figure 9.** Absolute azimuth deviations of most prominent peaks in the slowness spectra. Data from all frequencies are plotted. The data are plotted as a function of the interval they were obtained from: *P*, *PP*, *S* etc. denote intervals containing these waves; labels with suffix 'c' denote coda intervals. The dashed line indicates the resolution of GRF at period of 10 s.

authors observed a coda level that was independent of epicentral distance and decayed only slowly. Finally, the slowness diagrams of coda intervals show much energy concentrated at surface wave slownesses. This indicates that surface waves make up an appreciable part of the coda.

These results show that the first part of the long-period seismogram (up to and including the *PP/PPP*-waves) is consistent with the response of a laterally homogeneous body and that scattered waves, if any, are weak. The data in this part of the seismogram should be reproducible by some spherically symmetric Earth model. Although it is true that GRF is smaller than the dominant wavelengths present in this part of the data so that it is difficult to observe incoherencies, the results of the beamforming show that there is no significant amount of scattered energy present here. The observation that the *P* coda is coherent at a scale of 100 km (GRF) and that this coherence is lost at a scale of more than a few hundred kilometres (NARS), suggests that there exist lateral variations in the mantle on a scale comparable to the station separation of the NARS array. At the epicentral distances of the events in Table 1, the waves penetrate the mantle to a depth of about 1000 km, so these large-scale lateral variations must be situated in the upper mantle, assuming a largely homogeneous lower mantle. A recent stochastic analysis of global traveltimes data supports this assumption: a heterogeneous upper mantle and a low level of heterogeneity in the lower mantle (Gudmundsson, Davies & Clayton 1990). Fig. 1 also shows some great circle paths from event 2 to GRF and some NARS stations. The great circle paths to the NARS stations are so far apart that they may sample completely different tectonic regions. The large incoherency of the *P* coda is expected. Tomographic studies in Europe using *P*-wave delay times (Spakman 1988) or waveforms of the fundamental Rayleigh mode (Snieder 1988) also show large lateral variations in the upper mantle on a scale of several hundred kilometres, comparable to the NARS station separation.

The lateral heterogeneity is manifested in the intervals between the body wave phases. In these intervals GRF is smaller than the dominant wavelength in the data, making it easier to detect incoherencies in the wavefield. As scattered waves arrive from all azimuths, there is small coherence among the stations.

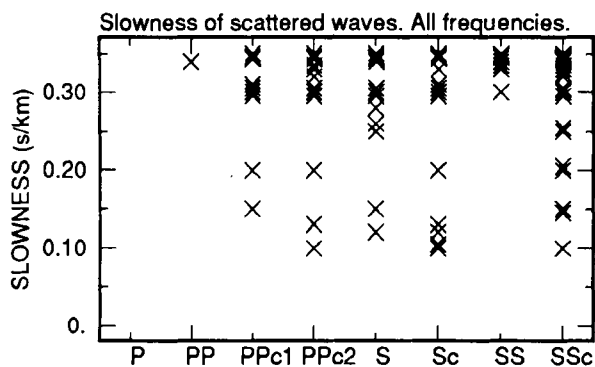


**Figure 10.** The slowness of the most prominent peaks in the slowness spectra, plotted in the same way as in Fig. 7. Energy peaks arriving along the great circle are not included. Note the concentration of data points at high slownesses, indicating that these waves are surface waves.

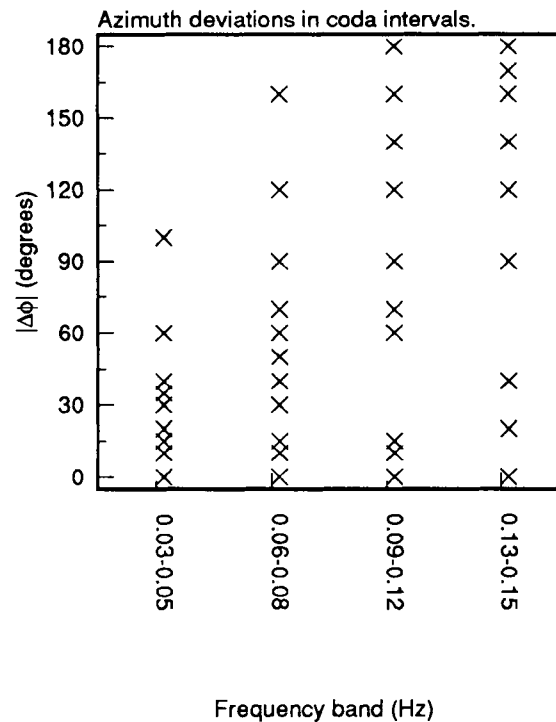


**Figure 11.** Absolute azimuth deviations as a function of frequency for data from coda intervals only. The deviations from back azimuth increase with increasing frequency.

### P CODA PREDICTED BY SPHERICALLY SYMMETRIC MODELS

The strong coherence of the *P* coda and the fact that no deviations from great circle azimuth could be detected suggest that a laterally homogeneous Earth model can be found that satisfies the data. A number of laterally homogeneous upper mantle models was taken from the literature to compute synthetic seismograms, to find out to what extent these models can explain the data. Only data from three superficial events (events 2, 3 and 4 in Table 1) are used, so that the *pP* and *sP* phases do not interfere with the *P* coda. In this case of only one source-receiver path for each event, the problem of non-uniqueness is large; it is not attempted to fit the data perfectly. A reflectivity code of Kennett (1988) was used, which ensures that the total response is obtained.

In order to quantify the differences between synthetics and data, two simple measures of this difference were calculated. One is the energy in the coda of *P*. As can be seen in Figs 3 and 5, the data show considerable energy in this interval. Ignoring scattering near the source, any candidate upper mantle model must be able to generate this amount of energy. As pointed out in the introduction, the signal from the 1-D earth between *P* and *PP* comprises top-side reverberations (with slightly higher slowness than that of *P*) and bottom-side reflections (with slowness slightly lower than that of *PP*) on the upper mantle discontinuities. Therefore, the energy in the *P* coda is normalized to the energy in both the *P*- and *PP*-waves:

$$f = \frac{|P\text{-coda}|^2}{|P\text{-wave}|^2 + |PP\text{-wave}|^2} \quad (1)$$

where  $| \cdot |^2$  denotes the energy in the interval between brackets. The value  $f$  can be thought of as a measure of the efficiency of a model to transfer energy of the  $P$  and  $PP$  phases into the  $P$  coda. As it is not a goal to model details in the data, the relative timing of any phases in the coda of  $P$  is of no interest. The  $P$  coda measure described here is independent of such timing differences.

Another quantitative measure of the difference between synthetics and data is the energy in the coherent part of the  $PP$  coda. Fig. 3 shows that the observed  $PP$  coda has reverberative characteristics and is reasonably coherent across the array up to about 600 s. The energy in the coherent part of the  $PP$  coda interval is normalized by the energy in the  $PP$  interval.

Reflectivity synthetics were computed for the following models: global models 1066B (Gilbert & Dziewonski 1975), PREM (Dziewonski & Anderson 1981) and PEMc (Dziewonski, Hales & Lapwood 1975) from normal mode data and body wave traveltimes; a number of local models derived from body wave form analysis: models S8 (Burdick 1981) and K8 (Given & Helmberger 1980) for western and eastern Europe, respectively; models SNA and TNA (Grand & Helmberger 1984), T9 (Burdick 1981) for the stable and tectonic parts of North America. If only one of  $P$  and  $S$  velocity was given, the other was calculated using the  $P/S$  ratio of PREM. All models, except the global models, were extended below the upper mantle with the lower mantle of PREM. The  $Q$  model given by Der, Lees & Cormier (1986) for shield areas under Eurasia derived from body wave data was used. The layer thickness was taken to be no more than 0.5 times the shortest wavelength at each depth [see Chapman & Orcutt (1985) and references therein for a discussion on this point]. The sampling of the slowness integral in the reflectivity calculations was always more than 10 points per shortest wavelength (Mallick & Frazer 1987). Both slowness and frequency integrals were tapered to avoid cut-off artifacts. The synthetics were then lowpassed at 0.15 Hz to remove acausal oscillations. The source mechanism was taken from the ISC bulletins. To keep computation times within limits, only events 2, 3 and 4 were considered, which are the nearest superficial events. The GRF instrument response was applied to the synthetics, which were then compared with the data.

Figures 12, 13 and 14 show a number of synthetics for each of the three events. The synthetics have been shifted in time to line up with the first onset in the data (bottom traces in Figs 12, 13 and 14, which represent the data from one of the stations of GRF). Table 2 lists the measures of  $P$  and  $PP$  coda energy.  $P$  and  $PP$  coda energy measures were obtained for the data as described in equation (1); for each event an average over all stations of GRF was obtained. The energy measures for the synthetics were normalized by these observed average energy measures. The data thus have a value of 1.0; a value lower than 1.0 means that the energy in the synthetics is lower than what is present in the data. The results for event 2 (Fig. 12) show that a number of models generate a  $P$  coda that is comparable to the data. The models are K8, PEMc and PREM. Model SNA predicts a coda that is too large. The other models do not fit the data well in this respect. Comparing the models, it turns out that the models that best fit the data all have a very thick lid (about 100 km) and a more or less pronounced low-velocity

zone (LVZ) in both  $P$  and  $S$  velocity. In these models, the jump in velocity at the base of the lid is about 2–4 per cent. Models with no LVZ or a very thin lid (as TNA, S8, T9) do not generate a sufficiently strong  $P$  coda.

Figure 13 and Table 2 show the results for event 3, which is quite close to event 2. The difference between the synthetics in Figs 12 and 13 is entirely due to the difference in epicentral distance. Synthetics calculated with an explosion source show very similar differences. As again models with a thick lid and a LVZ (SNA, PEMc; 1066B has a LVZ in the  $S$  velocity) show the best fit, the average upper mantle between GRF and the two events is essentially the same. The great circle paths are both within the stable shield areas in Europe (see Rial, Grand & Helmberger 1984).

The second quantitative measure is the length and amplitude of the coherent part of the  $PP$  coda. From Figs 12 and 13 it is apparent that the  $PP$  coda strongly depends on the model. From visual inspection and Table 2 it follows that PEMc seems the most appropriate model for the upper mantle between GRF and Hindu Kush. It should be noted here, that if a smaller  $P/S$  ratio is assumed for SNA, both the  $P$  and  $PP$  coda generated by SNA are much closer to the data. The models that fit the observed  $PP$  coda best are again characterized by a thick lid over a LVZ, with a more or less pronounced jump at the base of the lid.

Even 4 lies on the Mid-Atlantic Ridge (MAR). Synthetics and data are shown in Fig. 14. The data contain a  $PcP$  arrival at 650 s, which is not included in the synthetics. This will bias the results for the  $P$  coda fit to low values. Although this path is for the larger part oceanic, again a model with a thick lid and LVZ is found that explains the data best: the value of SNA in Table 2 is closest to 1. The average upper mantle here would not be expected to be similar to GCA (Walck 1984), which represents the upper mantle under a spreading centre, as only a minor part of the wave path is spent under such a structure. Model TNA is very similar to GCA and is listed in Table 2 with a reasonable energy content of the  $P$  coda, but this is due to the relatively low amplitude  $PP$ -waves. For this event all models fail to generate a  $PP$  coda level that is even near the very large amplitudes seen in the bottom trace in Fig. 14.

The results for the  $PP$  coda are not very stable. The three events are all within the  $PP$ -triplication distance, which causes a strong dependence on upper mantle structure of the  $PP$ -wavetrain. The  $PP$  coda is a  $PP$ -coupled  $PL$  mode (see, e.g. Alsop & Chander 1968); the reverberative characteristics of  $PP$ - $PL$  can be seen most clearly for event 2, see Fig. 3. It depends strongly on the crust and upper mantle above the LVZ near the receiver, as it is a leaky mode of this waveguide. This region of the upper mantle exhibits the strongest lateral variations in structure. This is the reason that the  $PP$ -waves and  $PP$  coda do not match observed  $PP$  and  $PP$  coda wavetrains. Table 2 shows that PEMc is always among the modes that predict a  $PP$  coda that is closest to the data with respect to its energy content; therefore PEMc also best represents the average structure of the upper mantle above the LVZ below GRF.

Both the  $P$  and  $PP$  coda observed in the data suggest an upper mantle with a thick lid over a more or less pronounced LVZ between GRF and Hindu Kush. This is in agreement with the results of Rial *et al.* (1984), who modelled  $S$ - and  $SS$ -waves for almost the same path as the

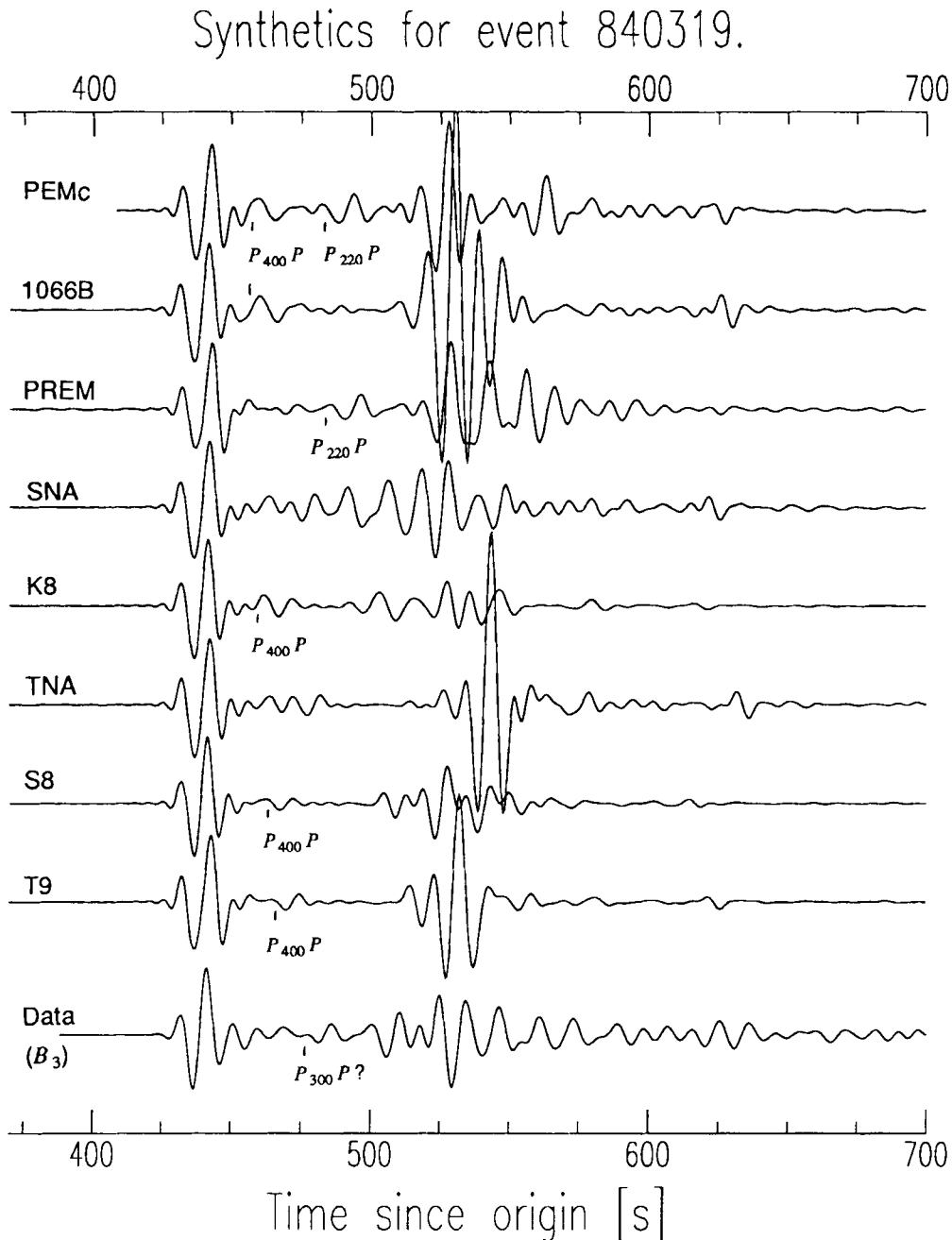


**Figure 12.** Reflectivity synthetics for a number of spherically symmetric upper mantle models. Bottom trace represents data from event 2 at GRF station B3. The synthetics have been shifted to line up the  $P$ -waves with the first onset in the data. Synthetics and data are low-passed at 0.15 Hz. The traces are normalized to the amplitude of the  $P$ -wave; some phases have been indicated.

present great circle path. They found that SNA modelled the data very well for predominantly shield paths, whereas TNA gave satisfactory results for tectonic paths. The boundary between these regions appeared to be very sharp. Paulssen (1988a) constructed a  $P$  and  $S$  velocity model of western Europe for events in the Mediterranean recorded by stations in Europe. This model is also very similar to SNA: it contains a thick lid over a pronounced LVZ. Given & Helmberger (1980), using Soviet nuclear explosions recorded in western Europe, constructed model K8 from waveform modelling. K8 has a relatively thin LVZ; although it generates a reasonable  $P$  coda, it hardly generates  $PP$

coda at all. The difference of the models K8 and PEMc is mainly the thickness of the LVZ.

It can thus be concluded that as far as  $P$  coda is concerned, no scattering is necessary to explain the data, at least at these frequencies and at this distance. The synthetics contain a coda comparable to the data; detailed characteristics are not explained. The one exception is event 4, that shows a  $P$  coda level larger than explained by any of the models used here, but this is also due to the  $PcP$  phase not included in the synthetics. With the synthetics presented here, scattering at or near the source cannot be discarded, as waves scattered near the source appear as coherent waves

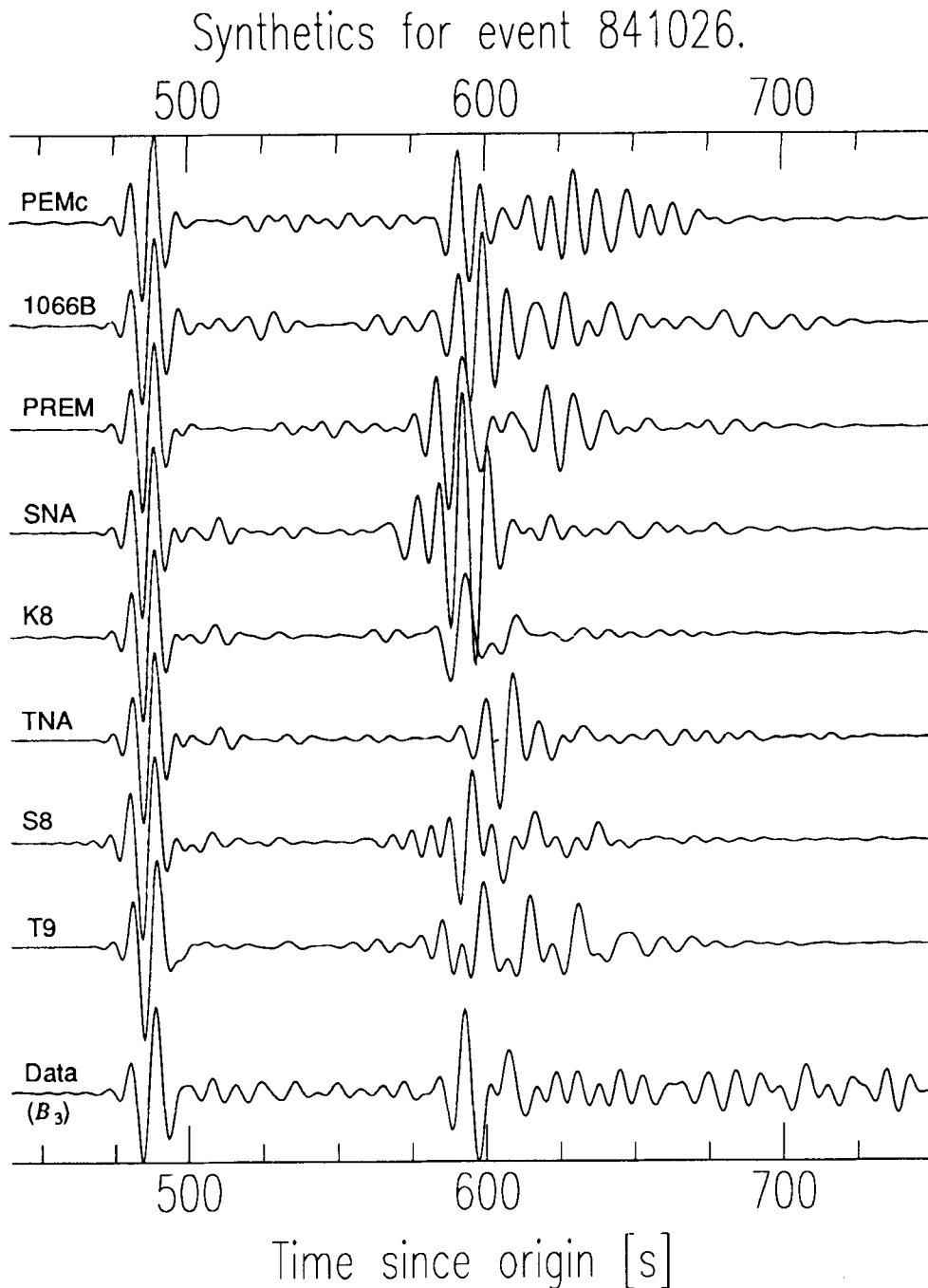


**Figure 13.** As Fig. 6, now for data from event 3 (GRF station B3).

near the receiver for suitably large distances. Greenfield (1971) showed that, for short-period  $P$  coda, Rayleigh waves scattered and converted to body waves by topography near the source could account for the observed decay of the coherent part of the coda. This may also account for the generally somewhat higher  $P$  coda level in the data.

#### UPPER MANTLE DISCONTINUITIES

Although it was not our intention to model individual phases, some constraints on upper mantle discontinuities can be obtained from a more detailed comparison of the synthetics and data in Figs 12, 13 and 14. Fig. 12 shows that

several models predict a pronounced  $P_{400}P$  phase at this epicentral distance. In the case of models 1066B and PEMc it is responsible for a considerable part of the energy of the  $P$  coda. These large amplitudes are not found in the data, indicating that in these models the discontinuities are probably too large. Even model K8, with a moderate velocity jump at 400 km and derived for a region near the present great circle path, generates a rather large  $P_{400}P$  phase; it is reproducible with WKB synthetics. A number of reasons for the small amplitude in the data can be thought of: the discontinuity can be weaker than in the model K8, which explains why bottom-side reflections are rarely reported in the literature (see e.g., Wajeman 1988;

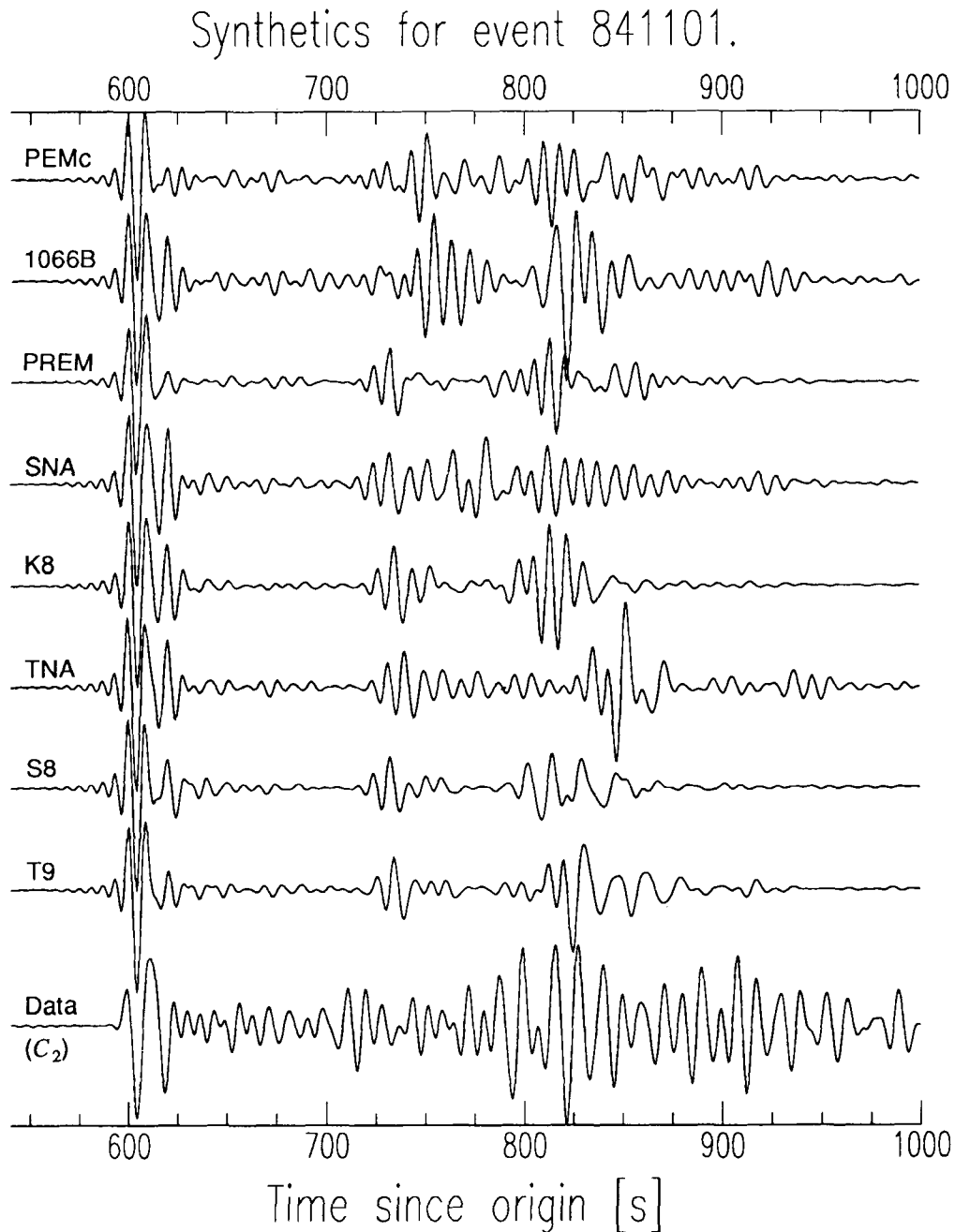


Figure 14. As Fig. 6, now for data from event 4 (GRF station C2).

Table 2. Measure of energy in P and PP coda.

Model	Event 2		Event 3		Event 4	
	P coda	PP coda	P coda	PP coda	P coda	PP coda
PEMc	0.82	0.79	0.43	0.90	0.13	0.27
1066B	0.13	0.02	0.34	0.32	0.27	0.17
PREM	0.57	1.66	0.29	0.25	0.05	0.08
SNA	2.72	0.33	0.41	0.14	0.46	0.19
K8	0.78	0.19	0.27	0.09	0.16	0.05
TNA	0.20	0.05	0.32	0.18	0.33	0.17
S8	0.25	0.25	0.23	0.24	0.16	0.19
T9	0.19	0.04	0.16	0.42	0.13	0.27
Data	1.00	1.00	1.00	1.00	1.00	1.00

Davis *et al.* 1989; Shearer 1990); the discontinuity exhibits lateral changes in strength [evidence for a laterally changing strength of the 670 km discontinuity is presented by Paulssen (1988b)]; the interface may be curved, causing focusing and defocusing of the *PdP* phase (Davis *et al.* 1989); other arrivals such as reverberations may mask the *PdP* phase; the synthetic phase may be in a caustic while the data are not; the discontinuity is not a first-order contrast, but rather a gradient with a thickness comparable to the wavelengths considered here. WKBJ synthetics showed that for model K8 the precursor is not a caustic, although it is within the triplication zone of the 670 km discontinuity. Ingate, Ha &

Muirhead (1986) show with numerical experiments that a velocity gradient with wavelength longer than about a quarter of the seismic wavelength is no longer 'seen' as an abrupt velocity jump. The low amplitude of the observed (rather: the unobserved)  $P_{400}P$  phase may then also be explained by the 400 km discontinuity being a gradient rather than a sharp contrast. This gradient would then have to have an extent of about 20–25 km, for a dominant frequency of 0.1 Hz.

Some models contain a strong 200 km discontinuity, like PREM and PEMc. The synthetic seismograms for these models show a strong pulse between the  $P_{400}P$  and  $PP$  phases. Such a pulse is not observed in the data, and it is likely that these models overestimate the strength of the 200 km discontinuity, which is in agreement with the result of Nolet (1990) for the  $S$  velocity contrast in western Europe. At these epicentral distances, no constraints can be put on the 670 discontinuity, as the  $P_{670}P$  phase arrives within the  $P$ - $pP$ - $sP$  wavetrain.

In Fig. 12 the data of station  $B_3$  show a strong phase arriving at about  $t = 480$  s, which is coherent across the array (Fig. 3). It arrives too late to be a  $P_{400}P$  phase. Assuming that it is a  $PdP$  phase, it corresponds with  $d$  about 300 km. This depth was also found by Wajeman (1988), for events near Japan recorded by the NARS array. The bounce point for this event is indicated with the open square in Fig. 1; it is near the Black Sea in the Caucasus. The results of Dercourt *et al.* (1986) indicate that subduction has been taking place for the last 200 Myr near this region. Remnants of

subducted material present in the upper mantle may cause anomalous phases such as this.

### SENSITIVITY TO LVZ STRUCTURE

The conclusion that models with a LVZ (in both  $P$  and  $S$  velocity) show a better fit of the data than models without a LVZ suggests the possibility of using the  $P$  coda to determine the presence or absence of a LVZ. The main arrivals associated with the LVZ are top- and bottom-side reflections at the top and base of the LVZ. Internal reverberations (peg-leg multiples) in the LVZ have very small amplitudes, about 0.1 per cent of that of  $P$ .

To determine the sensitivity of the  $P$  coda to LVZ structure, synthetic seismograms were computed for a number of models. PEMc was used as starting model, it has a LVZ in both  $P$  and  $S$  velocity. Models with no LVZ or a LVZ in only one of  $P$  and  $S$  velocity were constructed from it. The synthetics were computed with the reflectivity method. An explosion was used as source to ensure equal energy radiation in all directions.

The synthetic seismograms are plotted in Fig. 15, using the synthetic for the original PEMc as reference. The traces have been lined up at the  $P$ -wave for easier comparisons. No instrument response has been applied; the traces have been low-passed with corner frequency 0.15 Hz. Trace (a) in Fig. 15 shows the interval in the  $P$  coda where information from the LVZ arrives. The solid line is the total response, the dashed line represents the wavefield when only

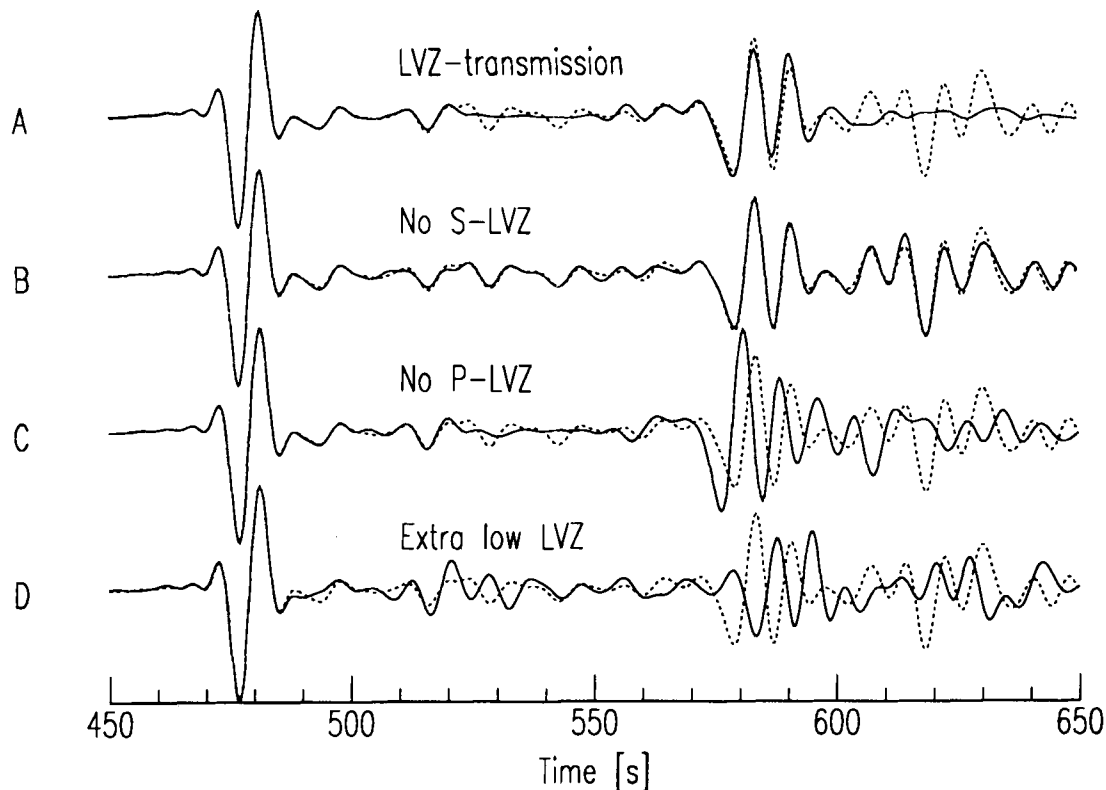


**Figure 15.** Reflectivity synthetics for model PEMc to test the sensitivity of the coda of  $P$  for LVZ structure. In all traces the dashed line represents the total response of the original model PEMc. (A) Solid line: PEMc with only transmission of energy through LVZ. (B) Solid line: PEMc, no LVZ in  $S$  velocity. (C) Solid line: PEMc, no LVZ in  $P$  velocity. (D) Solid line: PEMc, velocities in LVZ lowered by  $1 \text{ km s}^{-1}$ .

transmission through the LVZ is allowed. Top- and bottom-side reflections on the 220 km discontinuity, which marks the bottom of the LVZ, show up clearly. The interval with low amplitudes is the interval in which information from the LVZ should be looked for. Trace (b) in Fig. 15 shows the result for model PEMc without the LVZ in the *S* velocity (solid line; dashed line is the total response of the original PEMc). There are minor differences between the two traces, indicating low sensitivity of the *P* coda for the *S* velocity structure. Removing the LVZ in the *P* velocity has a large effect on the synthetics [trace (c) in Fig. 15, solid line is PEMc without a LVZ in *P* velocity, dashed line is original PEMc]. The synthetics in trace (c) show large amplitude differences. In trace (d) of Fig. 15, finally, the synthetic for PEMc with velocities in the LVZ lowered by  $1 \text{ km s}^{-1}$  is shown (solid line, dashed is original PEMc). Due to what is probably interference between the *P*400*P* and *P*p200*p* phases, there are large amplitudes around 520 s.

The results in Fig. 15 show that the long-period *P* coda is sensitive to the *P* velocity structure in the LVZ. Changes in the *S* velocity hardly affect the synthetics, indicating that *P*–*S* converted waves in the coda have small amplitude. This opens the possibility to use the phases in the *P* coda to monitor the *P* velocity structure of the LVZ. Such a conclusion had already been reached by Helmberger (1972) and York & Helmberger (1973), who studied *PL* propagation in the United States. They derived a map of lateral variations along the top of the upper mantle from the traveltime difference between *P* and *PL*. In this study *PdP* phases are used to probe the same region in the upper mantle. These phases have the advantage over *PL* that one is not restricted to events within about  $15^\circ$  to  $20^\circ$  from the station and that one can investigate regions on Earth where no earthquakes occur or stations are situated.

### FREQUENCY CONTENT OF CODA WAVES

In this and following sections the coda of *PP* (and *S*-waves) are considered. The frequency content of coda waves is a valuable source of information on scattering processes that act to produce the coda. Frequency losses due to absorption are ignored here. The frequency content of the *PP* coda is measured relative to that of the *PP*-waves by dividing the coda amplitude spectrum by the *PP*-wave amplitude spectrum. The latter was raised slightly to remove possible holes in the spectrum. This was then averaged over all stations of the array:

$$F(\omega) = \frac{1}{N} \sum_{i=1}^N \frac{PPc_i(\omega)}{PP_i(\omega) + \epsilon},$$

where  $PP_i(\omega)$  and  $PPc_i(\omega)$  are the Fourier transformed *PP* and *PP* coda intervals of station *i*, respectively;  $\epsilon$  is a small number; *N* is the number of stations (which is 13 for GRF). In this way, the source and receiver effects are cancelled.

Figure 16 shows two spectra of *PP* coda intervals, each divided by the *PP* amplitude spectrum. The spectra are the averages of the spectra of all 13 GRF stations. For most events, the spectra show low amplitudes for frequencies lower than about 0.2 Hz, whereas for higher frequencies the spectra are saturated. This is shown in Fig. 16(a). One exception is event 4, which shows an exceptionally large *PP* coda level [Fig. 16(b); for a time–distance plot see Fig. 5].

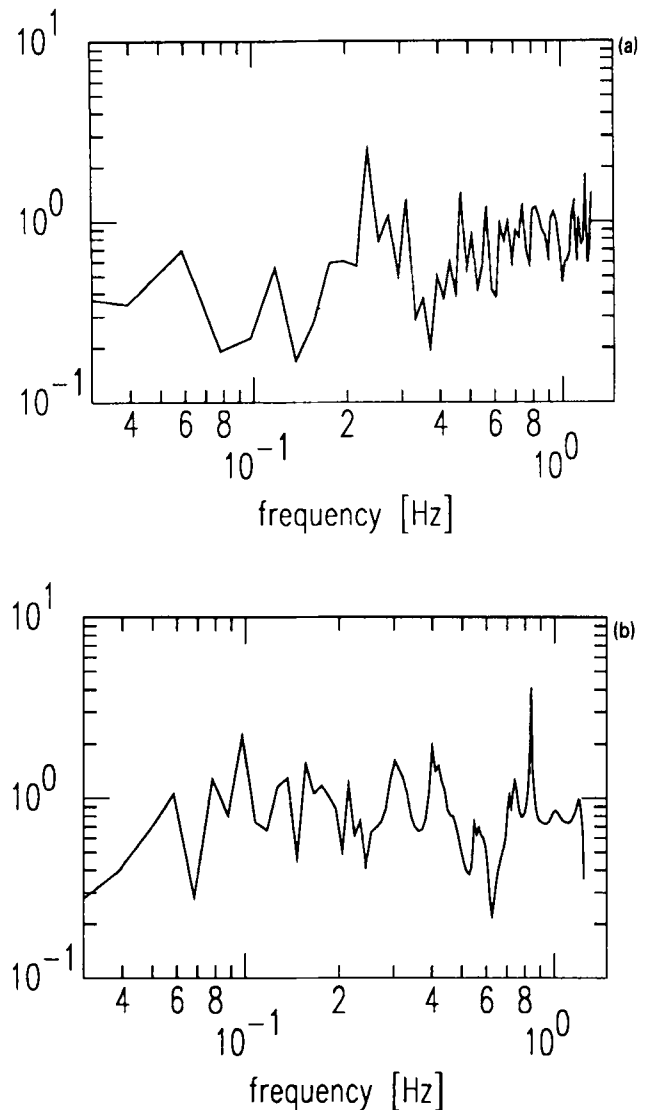


**Figure 16.** Spectra of *PP* coda intervals; the spectra are divided by the *PP*-wave spectra. (A) *PP* coda spectrum of event 2; (B) *PP* coda spectrum of event 4.

The spectrum in Fig. 16(a) shows that the frequencies higher than about 0.2 Hz are scattered more efficiently than lower frequencies. It is reasonable to assume that the frequencies of interest in this study, about 0.03–0.15 Hz, are within the weak scattering regime. Event 4 is the exception to the rule. This deviating observation will be explained in a later section. For higher frequencies the spectra are saturated, indicating strong multiple scattering. The frequency of 0.2 Hz is also the frequency at which microseisms have their peak energy. However, these will not influence the spectra, because the data have a very good *S/N* ratio (see Figs 3 and 5).

One can give an estimate of the lengthscale of the scatterers, responsible for the increase in coda level at 0.2 Hz. Seismic waves with frequency of 0.2 Hz have a wavelength of about 30–50 km in the upper mantle. As scatterers with lengthscales greater than that of the seismic wave have no influence on the wave, the scatterers responsible for the saturation above 0.2 Hz must have

length-scales equal to or shorter than 30–50 km. Assuming that at these frequencies the scattering occurs not far from the station, these structures would be situated in the crust. The next sections deal with the problem of explaining the scattering at lower frequencies.

### BODY WAVE SCATTERING

Scattering is important in the *PP* and *S* coda, and it would be interesting to see what kind of scatterers are necessary to explain these coda amplitudes. Let us for the moment ignore the beamforming results and let our working hypothesis be that the coda waves are body waves scattered from body waves near source or receiver. This is in the spirit of King *et al.* (1975), who showed that the scattering of *P*-waves near source or receiver is an adequate explanation of observed slowness and azimuth variations in high-frequency (above 0.6 Hz) *P* coda. The same mechanism may be at work at the lower frequencies studies here, and possibly the *PP* and *S* coda as well as in the *P* coda. Assuming this mechanism, we can try to estimate the scatterers necessary to explain the observed coda level. It is assumed that the Born approximation is valid: the waves are scattered only once. Elastic wave scattering theory of Wu & Aki (1985) is used to compute *P*→*P* and *P*→*S* scattered waves. The volume of the inhomogeneity is accounted for through the use of Mie scattering (which includes an integral over the inhomogeneity). The scattering structure is assumed to be a homogeneous sphere with constant perturbation in velocity or impedance. In all cases the most conservative estimate of scatterer strength is obtained by choosing the most efficient scattering configuration.

Scatterer size and strength are computed to explain a wave with an amplitude of 0.2 times the amplitude of the preceding body wave and frequency 0.10 Hz (which is representative of the coda level in Fig. 3), and arriving with a 50 s time lag. The results are presented in Fig. 17, as either velocity perturbations (forward scattering) or impedance perturbations (backward scattering) as a function of the product *ka*, seismic wavenumber times scalelength of the scatterer. The background velocity is taken to be 9 km s<sup>-1</sup>. It turns out that either unacceptable perturbations (>100 per cent) or unreasonable scalelengths (>1000 km) are necessary. *P*→*S* conversion appears to be more efficient than *P*→*P* scattering, but not efficient enough to explain the coda. The horizontal dashed line in Fig. 17 represents a 10 per cent perturbation, which can be assumed to be a reasonable perturbation. This level is reached only for very large scatterer size. For waves arriving at longer lapse times even stronger scatterers are needed, because the scattered wave has travelled longer distance and has therefore smaller amplitude. Thus, single scattering of body waves is not a likely mechanism to explain the *P* or *PP* coda at these periods.

Apparently, unrealistically strong scatterers are needed to explain the coda level. However, single scattering overestimates scatterer strength (Dubendorff & Menke 1980). Frankel & Wennerberg (1987) compared single and multiple scattering theory and showed that multiple scattering predicts a slower coda decay. In the present case, to obtain reasonable scatterer sizes and strengths, single scattering theory would have to overestimate the scatterers

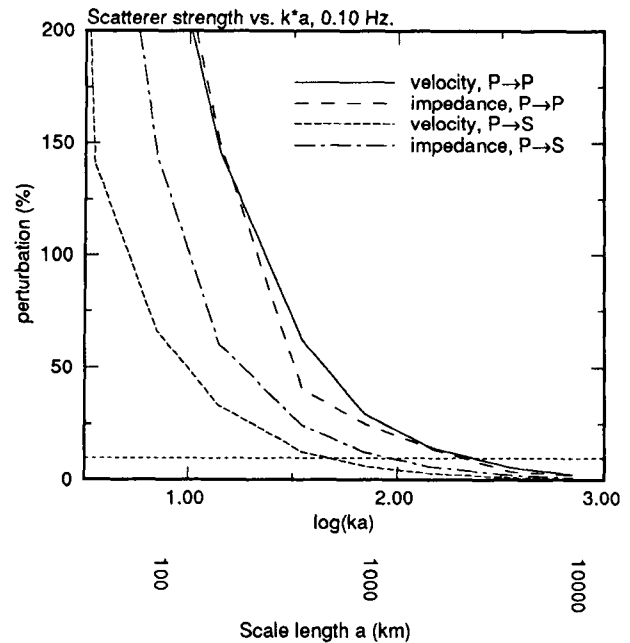


**Figure 17.** Strength of scatterer (either velocity or impedance perturbation) versus  $ka$ , seismic wavenumber times scatterer scalelength, for a wave with frequency 0.1 Hz, lapse time 50 s and amplitude 20 per cent of that of the direct wave. Epicentral distance is 4500 km. The scatterer is the most efficient scatterer on the ellipse focused on source and receiver. Calculated using the theory of Wu & Aki (1985). Results are for *P*→*P* and *P*→*S* scattering. The dashed horizontal line represents a perturbation of 10 per cent, which is assumed to be a reasonable value for inhomogeneities in the lithosphere.

by at least a factor of 10 and from the results of Frankel & Wennerberg (1987) it appears that this is unlikely.

Therefore, it appears that body wave to body wave scattering is not an adequate explanation of coda generation at the low frequencies studied here. This is in agreement with the beamforming results. This does not hold for higher frequencies (generally higher than about 1 Hz), as is shown by various authors mentioned before. In the next section the coupling of surface and body waves is studied and some linearized theories are applied to realistic scatterers.

### RAYLEIGH-TO-*P* COUPLING

The beamforming results indicate that the scattered waves in the *PP*- and *S*-wave coda are predominantly surface waves. These must have been excited by any of the earlier arriving body waves, as the signal-to-noise ratio is very good for most of the events. Prime candidate scatterers are surface topography and topography on the Moho; deeper heterogeneity will not contribute much to the scattering, as the Rayleigh waves at about 10 s do not penetrate very deep into the upper mantle. This explanation of body wave coda has been suggested earlier in the literature, for frequencies higher than 1 Hz (e.g. Key 1967; Greenfield 1971; Baumgardt 1985; Gupta, Lynnes & Wagner 1990). The coupling of Rayleigh to *P* has received much attention in experimental (e.g., McGarr & Alsop 1967; Gangi & Wesson 1978 and references therein) and numerical studies (e.g.

Fuyuki & Matsumoto 1980; Boore, Harmsen & Harding 1981; Hill & Levander 1984; Levander & Hill 1985; Stead & Helmberger 1988). From these studies it appears that reasonable inhomogeneity can explain scattered Rayleigh waves with amplitudes comparable to coda level observed here. It must be noted that all studies mentioned above are 2-D, so that Rayleigh waves do not suffer from geometrical spreading.

To investigate the efficiency of *P*-to-*R* coupling, theory on this subject was applied to realistic scatterers. The coupling due to topography on the Moho is treated by the theory of Odom (1986). The (linearized) theory is valid for an acoustic medium with small changes in the depth to the interface between a layer over a half-space. The model is a dipping Moho: a dip of 10 per cent over a distance of 200 km. This is a quite reasonable topography, it is common under western Europe (e.g. Meissner 1986; Luosto *et al.* 1990). Fig. 18 shows the amplitude of the converted guided mode (normalized by the amplitude of the plane incoming wave) as a function of both frequency and slowness of the direct wave. The results are independent of distance to the scatterer, as the direct wave is plane and the discrete mode is not affected by geometrical spreading. The figure shows that discrete modes with amplitudes of about 5 per cent of that of the direct wave are possible, ignoring the very large-amplitude mode that is excited by a *P*-wave travelling almost horizontally (slowness  $0.2 \text{ s km}^{-1}$ ). At higher frequencies the coupling is less efficient; this is because the penetration depth becomes shallower. It should be noted that the coupling may be weaker in an elastic medium, where the phase velocity of *P* is quite different from that of the Rayleigh modes. Therefore, this model probably overestimates the *P*-to-*R* coupling.

Gilbert & Knopoff (1960) described the *P*-to-*R* coupling due to surface topography in two dimensions. The 2-D model is an elastic half-space with a triangular hill, with 10 per cent sloping sides. The half-space has  $\alpha = 6$ ,  $\beta = 3.5$  and  $C_R = 3.4 \text{ km s}^{-1}$ , where  $C_R$  is the Rayleigh wave velocity. Fig. 19 shows the amplitude of the Rayleigh wave scattered from a plane *P*-wave (with amplitude 1), as a function of slowness of the plane direct wave. For this scatterer a

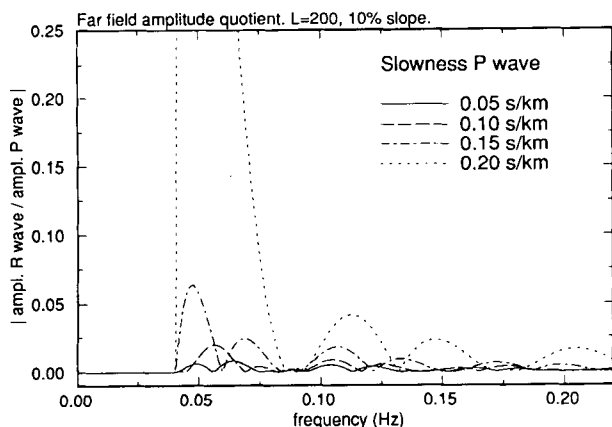


**Figure 18.** Amplitude of discrete mode excited by a *P*-wave of amplitude 1, as a function of frequency and slowness of the *P*-wave. The scatterer is a sloping Moho, the extent of the slope is 200 km, the slope is 10 per cent. The medium is 2-D and acoustic.

Rayleigh wave with an amplitude of 10 per cent of that of the *P*-wave is predicted.

A result for a similar scatterer in 3-D can be obtained with an extension to 3-D of Gilbert & Knopoff's theory due to Hudson (1967) and Hudson & Boore (1980). The 3-D scatterer is a Gaussian-shaped hill, with an area of  $20 \times 20 \text{ km}^2$  and a height of 1 km. The (plane) *P*-wave is vertically incident. The results are shown in Fig. 20. The results show that at a period of 10 s the coupling is most efficient. Due to geometrical spreading, the Rayleigh wave that has an amplitude (relative to *P*) of about 10 per cent very near the scatterer, quickly dies out to only 1 per cent at 100 km distance (this is indicated by the two curves in the plot).

From these simple calculations and the results presented in the literature, it appears that the *R*-to-*P* coupling in 2-D is quite efficient, especially at topography on the surface. Predicted Rayleigh wave amplitudes agree with those observed for realistic scatterers at frequencies of about 0.1 Hz. As there is no geometrical spreading, the coda thus created has a constant amplitude in time, assuming that there are enough scatterers and ignoring multiple scattering. The result for the 3-D Gaussian-shaped hill shows that the amplitude of the scattered waves quickly decays. However, a constant coda level is observed. The question is thus: do the increased number of scatterers and the increased strength of the scatterers (in 3-D a scatterer is measured by its volume instead of its area in 2-D) outweigh the stronger spreading in 3-D?

A simple argument shows that the increased number of scatterers indeed weighs up to the stronger geometrical spreading. The geometry of the problem in 3-D is sketched in Fig. 21. The receiver *R* is located inside a scattering region, in which the scatterers are assumed to be distributed randomly. A plane body wave crosses the region, exciting Rayleigh waves. The scatterers that contribute to the coda between lapse times  $t$  and  $t + \Delta t$  are approximately located on a circular region *E* focused on the receiver; *E* is bounded by circles of radius  $r = C_R t$  and  $r + \Delta r = C_R(t + \Delta t)$ , with  $C_R$  again the Rayleigh wave velocity. Now suppose that this region is filled entirely with Gaussian-shaped hills with half-width  $L$ . The number of scatterers inside the region *E* is then approximately  $2r \Delta r / L^2$ . At the receiver the scattered waves can be written as

$$u = \sum_i \frac{A_i}{\sqrt{r_i}} e^{i\phi_i} \quad (2)$$

where the sum is over all scatterers in *E* and the distance  $r_i$  is the distance scatterer–receiver. It is assumed that the amplitude of the body wave is the same at scatterer and receiver, so it does not enter the formula. This gives for the power

$$P = |u|^2 = \sum_i \sum_j \frac{A_i A_j^*}{\sqrt{r_i r_j}} e^{i(\phi_i - \phi_j)}. \quad (3)$$

Assuming the waves add randomly (this is justified if  $\Delta t$  is longer than the duration of individual scattered surface wavetrains) and that  $\Delta r \ll r$  a major contribution in the sum comes whenever  $i = j$ :

$$P \approx \sum_i \frac{|A_i|^2}{r_i} = n \frac{|A_i|^2}{r_i} = \frac{2\Delta r |A|^2}{L^2}. \quad (4)$$

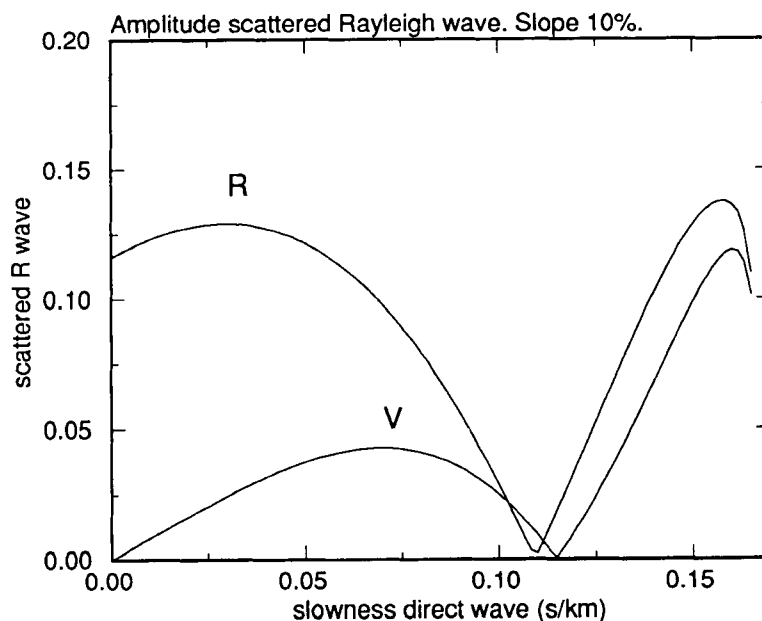


**Figure 19.** Amplitude of vertical and radial component of Rayleigh wave scattered from *P*-wave with amplitude 1, as a function of the slowness of the *P*-wave. The scatterer is a 2-D triangular hill, with 10 per cent sloping sides.

The power is now independent of the distance from scatterer to receiver and thus independent of lapse time. Using this expression and the theory of Hudson (1967) for the Gaussian-shaped hill, a (constant) coda level of about 10–15 per cent of that of the preceding body wave is found. This compares well with the value of about 20 per cent, commonly observed for the events in Table 1.

Thus, it is possible to explain the surface waves in the coda of *PP*- and *S*-waves as scattered from body waves. Surface topography alone can explain the greater part of the coda amplitude. It should be noted that at higher

frequencies the coupling at surface topography is even more efficient. [Using his 3-D theory, Hudson (1967) explained a Rayleigh wave observed in the short-period (about 1 Hz) coda of *P* at the Eskdalemuir array (Kay 1967) as excited by *P* at the slopes of a hill nearby the array.] Coupling at the Moho is probably weaker, but will increase the coda level. There are a number of assumptions in the above reasoning that affect the result. First, there are other possibilities of coupling Rayleigh to *P*. Coupling by volume heterogeneities, will increase the coda level. Unfortunately, there is no theory available treating volume scatterers, so their

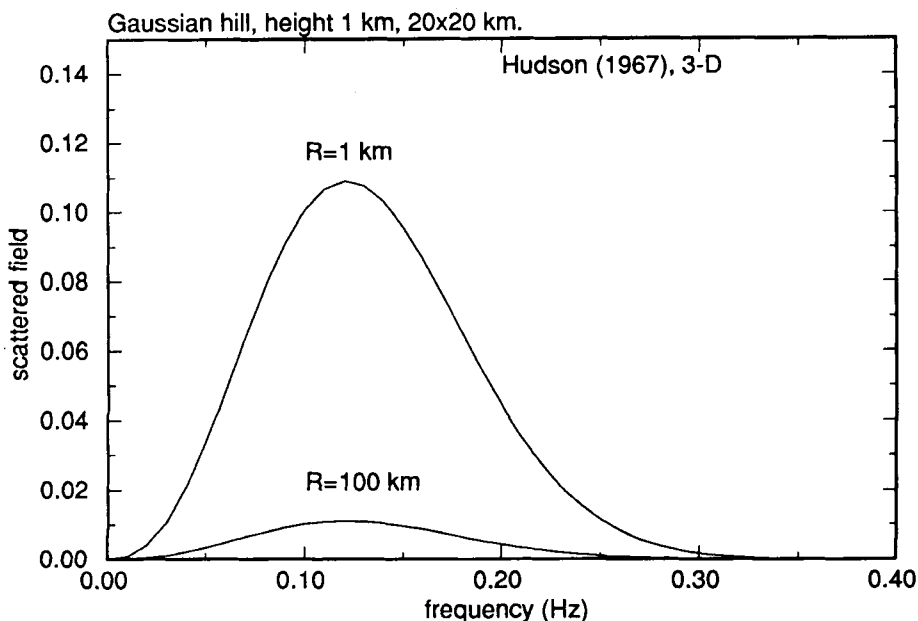


**Figure 20.** As Fig. 11, now for a 3-D Gaussian-shaped hill with height 1 km. The area of the hill is about  $20 \times 20 \text{ km}^2$ . Due to geometrical spreading, the Rayleigh wave quickly decays.

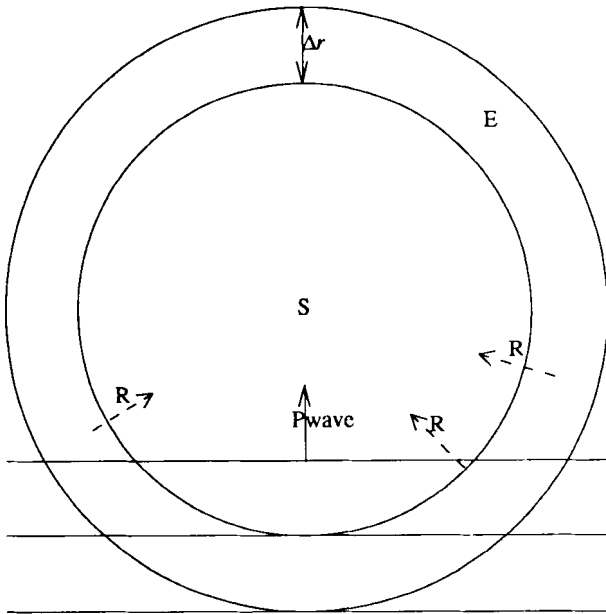


**Figure 21.** Geometry of the Rayleigh-to- $P$  coupling problem. A  $P$ -wave crosses the region, exciting Rayleigh waves at homogeneously distributed scatterers. Scattered waves arriving between lapse times  $t$  and  $t + \Delta t$  are located on a surface, which can be approximated by the surface  $E$  bounded by two circles focused on the station  $S$ . The width of the region  $E$  is  $\Delta r = \gamma \Delta t$ , where  $\gamma$  is the Rayleigh wave velocity.

importance is as yet unknown. Second, Hudson's theory is valid only for low-angle topography. Steep structures may cause a much larger coupling. Clearly there is need for theory that can handle strong scattering. Third, it is implicitly assumed that the Born approximation is valid for  $P$ -to- $R$  scattering; this is supported by the spectra shown in Fig. 16. This is not the case for the surface waves at the periods studied here (about 10 s). Snieder (1988) showed that for periods shorter than about 20 s the surface waves are in the strong scattering domain. Therefore, for sufficiently long lapse times, the surface waves in the body wave coda observed at GRF have had multiple interactions with the inhomogeneities between the point of excitation and GRF. This will cause a certain amount of energy to be scattered out of the coda system, e.g. by reverse coupling to body waves. Not accounting for this energy loss leads to underestimation of scatterer strength and/or size. Some of the surface waves recorded in the coda may have been scattered by heterogeneities that are essentially 2-D. Such structures near GRF include the Alps, ocean-continent boundaries and the Rhine Graben. Rayleigh waves thus scattered have a geometrical spreading that is much less than  $1/\sqrt{r}$ ; 2-D experiments presented in the literature (e.g. Boore *et al.* 1981) show that in this case it is not very difficult to obtain realistic Rayleigh wave amplitudes, even at long lapse times.

With the scattering argument the anomalously large  $PP$  coda amplitude of event 4 can be explained. This event lies very near the caustic in the  $PP$  triplication range (distance  $58.7^\circ$ ) where  $PP$ -waves arrive with large amplitude in a long time interval. Therefore, the  $PP$ -wavetrain is long and energetic. The  $PP$ -waves arrive consecutively (and thus do

not add their amplitudes) and each of them excites a long coda of scattered surface waves. These coda do overlap, creating a large-amplitude coda.

## DISCUSSION

The synthetic seismograms presented here prove that laterally homogeneous models of the upper mantle can explain the long-period  $P$ -wave coda at teleseismic distances. The scattering mechanism that is used to explain short-period  $P$  coda characteristics (such as amplitude decay, incoherency) is not needed to explain the long-period coda; it is also inconsistent with the observed coherency of the long-period  $P$  coda at GRF and the fact that beamforming analysis does not reveal any wave arriving off the great circle. As body wave to body wave scattering is quite inefficient, it is unlikely that there are scattered body waves in the  $P$  coda. This justifies the conclusion that the data from GRF represent the response from (some average of) the upper mantle between the event and GRF. The NARS array, on the other hand, shows hardly any coherency between two adjacent stations, even for stations at almost the same epicentral distance (see Fig. 4). Therefore, it can be concluded that the great circle paths from the events to the different NARS stations sample the lateral heterogeneity of the upper mantle under Europe. The GRF array apparently is too small. The scalelength of these lateral variations must be comparable to or larger than the average station separation of NARS. This constrains the scalelengths of the lateral heterogeneity of the upper mantle to be larger than a hundred to several hundreds of kilometres.

Combining the results presented here with earlier studies of the upper mantle under Europe suggests that the LVZ may be the origin of these lateral variations. The great circle paths studied by Given & Helmlberger (1980) and Rial *et al.* (1984) are closely spaced; the models proposed differ mainly in the thickness of the LVZ. Rial *et al.* further show that the boundary between tectonic and shield areas in Europe is probably quite sharp. These two areas are well modelled by the models TNA and SNA, respectively. The most prominent difference between these models is the absence in TNA of the well-pronounced LVZ of SNA. The results of Nolet (1990) show that the LVZ in  $S$  velocity that is present under the Iberian peninsula disappears beneath the Paris Basin and the Baltic shield. Snieder (1988) used a surface wave scattering formalism and found significant ( $\pm 5$  per cent) lateral variations at a depth of 100–200 km under Europe.

Although there are some upper mantle models that come close to the data as far as the energy content of the  $P$  coda is concerned, there is one characteristic that is matched by none of the synthetics. Fig. 5 most clearly shows the reverberative character of the long-period  $P$  coda. Whereas the synthetics have intervals of relatively low amplitude in between impulsive arrivals, there are no such pulse-like arrivals in the data. Again the explanation is the lateral heterogeneity of the upper mantle. The synthetics have been computed for identical structure beneath source and receiver. In this case reverberations have a multiplicity of more than one, and all equivalent reverberations (with the reverberation under either source or station) arrive at the

same time. If the source area structure differs from the receiver area structure, the multiplicity is lost and the reverberations can set up a reverberative *P* coda. This will also make it difficult to pick impulsive arrivals, such as *PdP* phases, as they are masked by the reverberations. When studying the *P* coda, one actually deals with three upper mantle structures, which are generally not identical: the structures beneath source and receiver and the upper mantle at the bounce point of the *PdP* phases. Resolving these three upper mantle structures is difficult, if not impossible with only a few source–station combinations. For the present problem the assumption of identical structures is definitely not correct. However, some constraints on what will represent an average upper mantle structure for the great circle paths studied can be found. That this is not an unreasonable assumption is shown by the agreement for the three events studied and by the agreement with this average structure and results reported in the literature for comparable great circle paths.

For the great circle paths studied here, the constraints that are found from synthetic seismogram analysis are a thick lid over a more or less pronounced, thick LVZ; models that do not have these features cannot explain the observed character (energy content) of the data. This suggests that the long-period *P* coda can be used to prove the existence or absence of a LVZ. Synthetic seismograms show that the *P* coda is more sensitive to *P* than to *S* velocity of the LVZ. The amplitude differences in the *P* coda correspond to top-side and bottom-side reflections at the bottom of the LVZ. Measuring the energy in the time interval in which arrivals from the LVZ are expected should make it possible to study the LVZ. Whereas the existence of a LVZ in the *S* velocity layer can be proven from surface wave dispersion, the LVZ in *P* velocity has not been proven unequivocally. Proving its existence or absence has important bearings on the structure and composition of the upper mantle. Estimates of the sharpness of the lower boundary of the LVZ can discriminate between theories concerning its origin, either partial melt, decreasing both *S* and *P* velocity (e.g. Anderson & Sammis 1970; Lambert & Wylie 1970; Stocker & Gordon 1975) or a simple pressure effect, causing the *S* velocity to decrease but the *P* velocity to increase (Tolstoy 1982).

One of the possible reasons for the null observation of the  $P_{400}P$  phase in the data is that the 400 km discontinuity is not an abrupt velocity increase, but a gradient of about 20–25 km thick, for a dominant period of 10 s. Although this is only one of several explanations for the null observation of this phase, it is interesting to compare this value with previously reported values for the thickness of the discontinuity. It compares well with high-pressure and high-temperature laboratory experiments from Katsura & Ito (1989), who estimate the velocity to increase over a depth interval of about 10–20 km, on the assumption that the discontinuity is caused by the olivine-modified spinel phase transition. From slowness and traveltimes analysis of short-period body wave data, Fukao (1977) estimated it to be 5–15 km, whereas Leven (1985) claimed a thickness of about 5 km under northern Australia.

The beamforming results show that the long-period coda of *PP*- and *S*-waves consist of scattered surface waves. 2-D experimental and numerical modelling results reported in

the literature and the simple calculations presented in this study suggest that the coupling of Rayleigh to *P*- or *S*-waves is efficient enough to excite a coda level comparable in strength and duration to observations. The 3-D coupling coefficients predicted by the theory of Hudson (1967) for a smooth topography at the surface ( $20 \times 20$  km<sup>2</sup> with a height of 1 km) agree well with observed coda amplitudes. When a dense, random coverage of such scatterers is assumed, a constant coda level can be explained, which is close to observed values. Such a dense coverage is not as unrealistic as it may seem, as a quick glance at topographic maps shows. The scatterer used here is in fact very smooth when compared to actual topography. Surface topography is not the only mechanism to couple Rayleigh to *P*-waves, but 2-D calculations suggest that coupling due to variations in Moho depth is not as efficient. Unfortunately, no theory is available that includes the coupling due to volume heterogeneities (e.g. in the crust). The shortcoming of the theories of both Hudson (1967) and Odom (1986) are that they are valid for smooth topography only. Clearly, a theory treating the scattering of body waves to surface waves at steep topography is needed. There is also the possibility that the greater part of the observed scattered surface waves is actually scattered by obstacles that are essentially 2-D, as e.g. ocean–continent boundaries, mountain chains. Such waves have a much less severe geometrical spreading than waves scattered by a feature that is finite (as compared to the wavelength) in both horizontal directions. It is not expected that body wave to body wave scattering contributes a significant amount to the coda level; in order to cause a scattered wave of reasonable amplitude either unacceptably large scattering volumes or unacceptably strong scatterers are needed. This is in agreement with the observation that very few scattered waves have a body wave slowness.

Explaining the *PP*- and *S*-wave coda as scattered surface waves raises the question why such waves are not observed in the long-period coda of *P*. For short periods scattered surface waves are observed after *P* (Key 1967; Langston 1989; Gupta *et al.* 1990). The explanation is given by the reflectivity synthetics shown in Figs 12, 13 and 14. The synthetics show that the signal from the spherically symmetric Earth is rather strong between *P* and *PP*. There is hardly such signal after the *PP*/*PPP*-wavetrain, although the slowness interval that was selected contained slownesses up to that of the *S*-wave. Therefore, the coherent signal of the 1-D Earth may obscure scattered waves between *P* and *PP*, but after *PP* there is no such signal. It must also be noted that as nearly all events are within the *PP* triplication distance, the *PP* coda is caused by more than one *PP*-wave, whereas all scattered waves arriving before *PP* are scattered from a single *P*-wave. Furthermore, the coupling between Rayleigh and *P* is not as efficient as that between Rayleigh and *PP*. This can be seen in Fig. 18. The Rayleigh wave amplitude increases with increasing slowness at fixed frequency, away from the nodes in the individual curves.

In contrast with the long-period coda of *P*, from which information about the layered structure of the upper mantle can be derived, the scattered surface waves carry only information about lateral heterogeneity of the crust and possibly the lithosphere, at long periods. It is not feasible to extract deterministic characteristics of the scatterers from

the coda, such as location and/or scalelength and strength. This is due to the intrinsic complexity of scattered coda waves. At any moment in the coda interval there are scattered waves arriving from possibly all azimuths. More specifically, at any moment there is probably more than one wave arriving from the same azimuth. Such a complex wavefield cannot be handled in a deterministic way. A statistical approach would be more fruitful. However, one obtains information about the crust only, and, judging from the efficiency of *R*-to-*P* coupling at surface topography, mainly about surface features. Of course there are more efficient ways to obtain such information.

## ACKNOWLEDGMENTS

We thank G. Nolet for helpful discussions and for critically reading the manuscript. The constructive remarks of an anonymous referee are highly appreciated.

## REFERENCES

- Aki, K., 1973. Scattering of *P* waves under the Montana Lasa, *J. geophys. Res.*, **78**, 1335–1346.
- Aki, K. & Chouet, B., 1975. Origin of coda waves: source, attenuation and scattering effects, *J. geophys. Res.*, **80**, 3322–3342.
- Aki, K. & Richards, P. G., 1980. *Quantitative Seismology*, Freeman, San Francisco.
- Alsop, L. E. & Chander, R., 1968. The generation of direct and coupled *PL* modes, *Suppl. Nuovo Cimento*, **6**, 7–21.
- Anderson, D. L. & Sammis, C., 1970. Partial melting in the upper mantle, *Phys. Earth planet. Inter.*, **3**, 41–50.
- Baag, C.-E. & Langston, C. A., 1985. Shear-coupled *PL*, *Geophys. J. R. astr. Soc.*, **80**, 363–385.
- Backus, G. & Gilbert, F., 1968. The resolving power of gross Earth data, *Geophys. J. R. astr. Soc.*, **16**, 169–205.
- Barley, B. J., Hudson, J. A. & Douglas, A., 1982. *S* to *P* scattering at the 650-km discontinuity, *Geophys. J. R. astr. Soc.*, **69**, 159–172.
- Baumgardt, D. R., 1985. Comparative analysis of teleseismic *P*-coda and *Lg* wave from underground nuclear explosions in Eurasia, *Bull. seism. Soc. Am.*, **75**, 1413–1433.
- Bolt, B. A., 1970. *PdP* and *PKiKP* waves and diffracted *PcP* waves, *Geophys. J. R. astr. Soc.*, **20**, 367–382.
- Boore, D. M., Harmsen, S. C. & Harding, S. T., 1981. Wave scattering from a step change in surface topography, *Bull. seism. Soc. Am.*, **71**, 117–125.
- Bostock, M. G. & Kennett, B. L. N., 1990. The effect of 3-D structure on *Lg* propagation patterns, *Geophys. J. Int.*, **101**, 355–365.
- Bouchon, M., 1982. The complete synthesis of seismic crustal phases at regional distances, *J. geophys. Res.*, **87**, 1735–1742.
- Bungum, H. & Capon, J., 1974. Coda pattern and multipath propagation of Rayleigh waves at NORSAR, *Phys. Earth planet. Inter.*, **9**, 111–127.
- Burdick, L. J., 1981. A comparison of the upper mantle structure beneath North America and Europe, *J. geophys. Res.*, **86**, 5926–5936.
- Capon, J., 1969. High resolution frequency–wavenumber spectrum analysis, *Proc. IEEE*, **57**, 1408–1418.
- Capon, J., 1970. Analysis of Rayleigh-wave multipath propagation at LASA, *Bull. seism. Soc. Am.*, **60**, 1701–1731.
- Chapman, C. H. & Orcutt, J. A., 1985. The computation of body wave synthetic seismograms in laterally homogeneous media, *Rev. Geophys.*, **23**, 105–163.
- Davis, J. P., Kind, R. & Sacks, I. S., 1989. Precursors to *P'P'* re-examined using broad-band data, *Geophys. J. Int.*, **99**, 595–604.
- Der, Z. A., Lees, A. C. & Cormier, V. F., 1986. Frequency dependence of *Q* in the mantle underlying the shield areas of Eurasia, part III: the *Q* model, *Geophys. J. R. astr. Soc.*, **87**, 1103–1112.
- Dercourt, J. *et al.*, 1986. Geological evolution of the Tethys belt from the Atlantic to the Pamirs since the Lias, *Tectonophysics*, **123**, 241–315.
- Dost, B., 1990. Upper mantle structure under western Europe from fundamental and higher mode surface waves using the NARS array, *Geophys. J. Int.*, **100**, 131–151.
- Dubendorff, B. & Menke, W., 1989. Time-domain apparent-attenuation operators for compressional and shear waves: experiment versus single-scattering theory, *J. geophys. Res.*, **91**, 14 023–14 032.
- Dziewonski, A. M. & Anderson, D. L., 1981. Preliminary reference Earth model, *Phys. Earth planet. Inter.*, **25**, 297–356.
- Dziewonski, A. M., Hales, A. & Lapwood, E., 1975. Parametrically simple Earth models consistent with geophysical data, *Phys. Earth planet. Inter.*, **10**, 12–48.
- Flatté, S. M. & Wu, R.-S., 1988. Small-scale structure in the lithosphere and asthenosphere deduced from arrival time and amplitude fluctuations at NORSAR, *J. geophys. Res.*, **93**, 6601–6614.
- Frankel, A. & Clayton, R. W., 1986. Finite difference simulations of seismic scattering: implications for the propagation of short-period seismic waves in the crust and models of crustal heterogeneity, *J. geophys. Res.*, **94**, 6465–6489.
- Frankel, A. & Wennerberg, L., 1987. Energy-flux model of seismic coda: separation of scattering and intrinsic attenuation, *Bull. seism. Soc. Am.*, **77**, 1223–1251.
- Fukao, Y., 1977. Upper mantle *P* structure on the ocean side of the Japan–Kurile arc, *Geophys. J. R. astr. Soc.*, **50**, 621–642.
- Fuyuki, M. & Matsumoto, Y., 1980. Finite-difference analysis of Rayleigh wave scattering at a trench, *Bull. seism. Soc. Am.*, **70**, 2051–2070.
- Gangi, A. F. & Wesson, R. L., 1978. *P*-wave to Rayleigh-wave conversion coefficients for wedge corners: model experiments, *J. Comp. Phys.*, **29**, 370–388.
- Gao, L. S., Lee, L. C., Biswas, N. N. & Aki, K., 1983. Comparison of the effect between single and multiple scattering on coda waves for local earthquakes, *Bull. seism. Soc. Am.*, **73**, 377–389.
- Gilbert, F. & Knopoff, L., 1960. Seismic scattering from topographic irregularities, *J. geophys. Res.*, **65**, 3437–3444.
- Gilbert, F. & Dziewonski, A. M., 1975. An application of normal mode theory to the retrieval of structural parameters and source mechanisms from seismic spectra, *Phil. Trans. R. Soc. Lond.*, **A**, **278**, 187–269.
- Given, J. W. & Helmberger, D. V., 1980. Upper mantle structure of northwestern Eurasia, *J. geophys. Res.*, **85**, 7183–7194.
- Grand, S. P. & Helmberger, D. V., 1984. Upper mantle shear structure of North America, *Geophys. J. R. astr. Soc.*, **76**, 399–438.
- Greenfield, R. J., 1971. Short-period *P*-wave generation by Rayleigh-wave scattering at Novaya Zemlaya, *J. geophys. Res.*, **76**, 7988–8002.
- Gudmundsson, O., Davies, J. H. & Clayton, R. W., 1990. Stochastic analysis of global traveltimes data: mantle heterogeneity and random errors in the ISC data, *Geophys. J. Int.*, **102**, 25–43.
- Gupta, I. N., Lynnes, C. S. & Wagner, R. A., 1990. Broadband *f*–*k* analysis of array data to identify sources of local scattering, *Geophys. J. R. astr. Soc.*, **17**, 183–186.
- Gutowski, P. R. & Kanasewich, E. R., 1974. Velocity spectral evidence of upper mantle discontinuities, *Geophys. J. R. astr. Soc.*, **36**, 21–32.

- Helmberger, D. V., 1972. Long-period body wave propagation from 4° to 13°, *Bull. seism. Soc. Am.*, **62**, 325–341.
- Helmberger, D. V. & Engen, G. R., 1980. Modelling the long-period body waves from shallow earthquakes at regional ranges, *Bull. seism. Soc. Am.*, **70**, 1699–1714.
- Hill, N. R. & Levander, A. R., 1984. Resonances of low-velocity layers with lateral variations, *Bull. seism. Soc. Am.*, **74**, 521–537.
- Högbom, J. A., 1974. Aperture synthesis with a non-regular distribution of interferometer baselines, *Astr. Astrophys. Suppl.*, **15**, 417–426.
- Hudson, J. A., 1967. Scattered surface waves from a surface obstacle, *Geophys. J. R. astr. Soc.*, **13**, 441–458.
- Hudson, J. A. & Boore, D. M., 1980. Comments on 'Scattered surface waves from a surface obstacle' by J. A. Hudson, *Geophys. J. R. astr. Soc.*, **60**, 123–127.
- Husebye, E. S. & Madariaga, R., 1970. The origin of precursors to core waves, *Bull. seism. Soc. Am.*, **60**, 939–952.
- Husebye, E., Haddon, R. A. W. & King, D. W., 1977. Precursors to  $P'P'$  and upper mantle discontinuities, *J. Geophys.*, **43**, 535–543.
- Ingate, S. F., Ha, J. & Muirhead, K. J., 1986. Limitations on waveform modelling of long-period seismograms, *Geophys. J. R. astr. Soc.*, **86**, 57–61.
- Katsura, T. & Ito, E., 1989. The system  $Mg_2SiO_4$ – $Fe_2SiO_4$  at high pressures and temperatures: precise determination of stabilities of olivine, modified spinel and spinel, *J. geophys. Res.*, **94**, 15 663–15 670.
- Kennett, B. L. N., 1987. Observational and theoretical constraints on crustal and upper mantle heterogeneity, *Phys. Earth planet. Inter.*, **47**, 319–332.
- Kennett, B. L. N., 1988. Systematic approximations to the seismic wavefield, in *Seismological Algorithms*, pp. 237–259, ed. Doornbos, D. J., Academic Press, London.
- Key, F. A., 1967. A signal-generated noise recorded at the Eskdalemuir Seismometer Array Station, *Bull. seism. Soc. Am.*, **57**, 27–38.
- Kind, R. & Vinnik, L. P., 1988. The upper mantle discontinuities underneath the GRF array from  $P$ -to- $S$  converted phases, *J. Geophys.*, **62**, 138–147.
- King, D. W., Haddon, R. A. W. & Husebye, E. S., 1975. Precursors to  $PP$ , *Phys. Earth planet. Inter.*, **10**, 103–127.
- Korn, M., 1988.  $P$ -wave coda analysis of short-period array data and the scattering and absorptive properties of the lithosphere, *Geophys. J.*, **93**, 437–449.
- Lambert, I. B. & Wylie, P. J., 1970. Low-velocity zone of the Earth's mantle: incipient melting caused by water, *Science*, **169**, 764–766.
- Langston, C. A., 1989. Scattering of teleseismic body waves under Pasadena, California, *J. geophys. Res.*, **94**, 1935–1951.
- Levander, A. R. & Hill, N. R., 1985.  $P$ – $SV$  resonances in irregular low-velocity surface layers, *Bull. seism. Soc. Am.*, **75**, 847–864.
- Leven, J. H., 1985. The application of synthetic seismograms to the interpretation of the upper mantle  $P$ -wave velocity structure in northern Australia, *Phys. Earth planet. Inter.*, **38**, 9–27.
- Levshin, A. & Berteussen, K.-A., 1979. Anomalous propagation of surface waves in the Barents Sea as inferred from NORSAR recordings, *Geophys. J. R. astr. Soc.*, **56**, 97–118.
- Luosto, U. *et al.*, 1990. Crust and upper mantle structure along the DSS profile in SE Finland, *Geophys. J. Int.*, **101**, 89–110.
- Mallick, S. & Frazer, L. N., 1987. Practical aspects of reflectivity modelling, *Geophysics*, **52**, 1355–1364.
- McGarr, A. & Alsop, L. E., 1967. Transmission and reflection of Rayleigh waves at vertical boundaries, *J. geophys. Res.*, **72**, 2169–2180.
- Meissner, R., 1986. *The Continental Crust, a Geophysical Approach*, Academic Press, Orlando, FL.
- Nakanishi, I., 1988. Reflections of  $P'P'$  from upper mantle discontinuities beneath the Mid-Atlantic ridge, *Geophys. J.*, **93**, 335–346.
- Nolet, G., 1990. Partitioned waveform inversion and two-dimensional structure under the network of autonomously recording seismographs, *J. geophys. Res.*, **95**, 8499–8512.
- Odom, R., 1986. A coupled mode examination of irregular waveguides including the continuum spectrum, *Geophys. J. R. astr. Soc.*, **86**, 425–453.
- Oliver, J. & Major, M., 1960. Leaking modes and the PL phase, *Bull. seism. Soc. Am.*, **50**, 165–180.
- Palmer, D. R., Brown, M. G., Tappert, F. D. & Bezdek, H. F., 1988. Classical chaos in nonseparable wave propagation problems, *Geophys. Res. Lett.*, **15**, 569–572.
- Paulssen, H., 1985. Upper mantle converted waves beneath the NARS array, *Geophys. Res. Lett.*, **12**, 709–712.
- Paulssen, H., 1988a. Lateral heterogeneity of Europe's upper mantle as inferred from modelling of broad-band body waves, *Geophys. J. R. astr. Soc.*, **91**, 171–199.
- Paulssen, H., 1988b. Evidence for a sharp 670-km discontinuity as inferred from  $P$  to  $S$  converted waves, *J. geophys. Res.*, **93**, 10 489–10 500.
- Rial, J. A., Grand, S. & Helmberger, D. V., 1984. A note on lateral variation in upper-mantle shear velocity across the Alpine front, *Geophys. J. R. astr. Soc.*, **77**, 639–654.
- Sato, H., 1984. Attenuation and envelope formation of three-component seismograms of small local earthquakes in randomly inhomogeneous lithosphere, *J. geophys. Res.*, **89**, 1221–1241.
- Sereno, T. J. & Orcutt, J. A., 1988. Synthetic  $P_n$  and  $S_n$  phases and the frequency of  $Q$  of oceanic lithosphere, *J. geophys. Res.*, **92**, 3541–3566.
- Shearer, P., 1990. Seismic imaging of upper mantle structure—new evidence for a 520 km discontinuity, *Nature*, **344**, 121–126.
- Snieder, R., 1988. Large scale waveform inversions of surface waves for lateral heterogeneity—II: Application to surface waves in Europe and the Mediterranean, *J. geophys. Res.*, **93**, 12 067–12 080.
- Spakman, W., 1988. Upper mantle delay time tomography, *PhD thesis*, University of Utrecht, Utrecht, The Netherlands.
- Stead, R. J. & Helmberger, D. V., 1988. Numerical-analytical interfacing in two dimensions with applications to modelling NTS seismograms, *PAGEOPH*, **128**, 157–193.
- Stocker, R. L. & Gordon, R. B., 1975. Velocity and internal friction in partial melts, *J. geophys. Res.*, **80**, 4828–4836.
- Toksöz, M. N., Dainty, A. M. & Charrette, E. E., 1989. Coherency of ground motion at regional distances and scattering, *Phys. Earth planet. Inter.*, submitted.
- Tolstoy, I., 1982. On elastic waves in prestressed solids, *J. geophys. Res.*, **87**, 6823–6827.
- Wajeman, N., 1988. Detection of underside  $P$  reflections at mantle discontinuities by stacking broadband data, *Geophys. Res. Lett.*, **15**, 669–672.
- Walck, M. C., 1984. The  $P$ -wave upper mantle structure beneath an active spreading centre: the gulf of California, *Geophys. J. R. astr. Soc.*, **76**, 697–723.
- Whitcomb, J. H. & Anderson, D. L., 1970. Reflection of  $P'P'$  seismic waves from discontinuities in the mantle, *J. geophys. Res.*, **75**, 5713–5728.
- Wu, R. & Aki, K., 1985. Elastic wave scattering by a random medium and the small-scale inhomogeneities in the lithosphere, *J. geophys. Res.*, **90**, 10 261–10 273.
- York, J. E. & Helmberger, D. V., 1973. Low-velocity zone variations in the southwestern United States, *J. geophys. Res.*, **78**, 1883–1886.

## APPENDIX A: BEAMFORMING

Suppose we have  $K$  stations with recorded time series  $s_j(t)$  and Fourier transforms of these traces  $S_j(\omega)$ . We wish to

find the spectrum of slownesses present in the wavefield. The relation between the data  $S_j(\omega)$  and the slowness spectrum is

$$S_j(\omega) = \int_{-\infty}^{\infty} P(\mathbf{p}) e^{-i\omega \mathbf{p} \cdot \mathbf{r}_j} d^2p, \quad (\text{A0})$$

where  $P(\mathbf{p})$  is the true slowness spectrum,  $\mathbf{p}$  is the horizontal slowness vector and  $\mathbf{r}_j$  is the vector pointing from a reference point (e.g. the centre of the array) to station  $j$ . The factor  $\exp(-i\omega \mathbf{p} \cdot \mathbf{r}_j)$  is the phase shift, relative to the reference point, of a wave with slowness  $\mathbf{p}$  due to the distance  $\mathbf{r}_j$  projected on the direction of the slowness  $\mathbf{p}$ . The integration limits are in practice not infinity; a suitable upper limit may be chosen, based on physically expected minimum velocities. The simplest estimate  $\hat{P}$  of the true slowness spectrum  $P(\omega, \mathbf{p})$  at frequency  $\omega$  is just a sum of the data  $S_j(\omega)$ , each delayed with a phase delay of  $\omega \mathbf{p} \cdot \mathbf{r}_j$ ,

$$\hat{P}(\omega, \mathbf{p}) = \sum_{j=1}^K w_j S_j(\omega) e^{i\omega \mathbf{p} \cdot \mathbf{r}_j}. \quad (\text{A1})$$

Weights  $w_j$  can be used to control the slowness resolution; in the conventional beamforming technique these are set to 1. The components  $S_j$  are normalized to unit length to avoid artifacts due to uneven station calibration or amplitude variations across the array. In the slowness spectra shown in this paper, the spectra have been averaged for a given frequency interval:

$$\int_{\omega_1}^{\omega_2} |\hat{P}(\omega, \mathbf{p})|^2 d\omega. \quad (\text{A2})$$

The array response is obtained by inserting a monochromatic wave in (A1). For a wave with slowness  $\mathbf{p}_0$ , we have  $S_j = \exp(-i\omega \mathbf{p}_0 \cdot \mathbf{r}_j)$  and the array response is then simply

$$R(\mathbf{p}, \mathbf{p}_0) = \sum_{j=1}^K w_j e^{i\omega(\mathbf{p} - \mathbf{p}_0) \cdot \mathbf{r}_j}. \quad (\text{A3})$$

The array response obtained with the conventional method for a frequency of 0.05 Hz and a vertically incident wave is shown in Fig. A1(a). The shape of the array is reflected in its array response: elongated in the E–W direction, the direction in which the array is narrowest. The presence of side lobes and the finiteness of the main lobe are the result of the finite sampling in space of the wavefield.

The resolving power of this method is poor, so there is need for an improvement. Equation (A0) can be viewed as a linear inverse problem of the form  $\mathbf{d} = \mathbf{G}\mathbf{m}$  (dropping integrals), where  $\mathbf{G}$  is some operator [in this case  $\exp(-i\omega \mathbf{p} \cdot \mathbf{r}_j)$ ] acting on the real model  $\mathbf{m}$  (the slowness field) to yield the data vector  $\mathbf{d}$  [ $S_j(\omega)$ , the phase of frequency  $\omega$  at station  $j$ ]. The problem is now to find the best possible estimate  $\hat{\mathbf{m}}$  of the real model  $\mathbf{m}$ . The theory due to Backus & Gilbert (1968) can be applied here.

The data  $\mathbf{d}$  are related to the true spectrum  $P(\mathbf{p})$  through an operator  $\mathbf{G}(\mathbf{p})$  (replacing the integration limits by an estimated maximum slowness  $p_{\max}$ )

$$\mathbf{d} = \iint_{|\mathbf{p}| \leq p_{\max}} \mathbf{G}(\mathbf{p}) P(\mathbf{p}) d^2p \quad (\text{A4})$$

with  $\mathbf{G}$ ,  $P$  and  $d$  as described above. The estimate  $\hat{P}(\mathbf{p})$  is

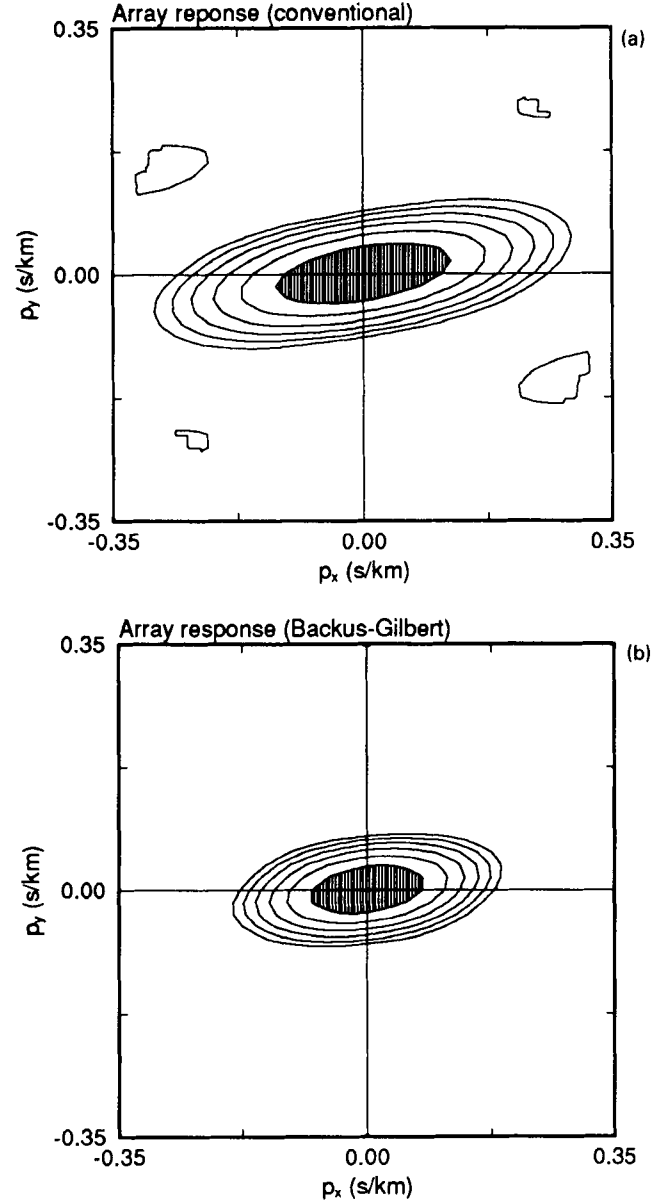


**Figure A1.** Array response of GRF. (a) Response with the conventional beam forming method. Two side lobes can just be seen at the edges of the spectrum. (b) Response obtained with the Backus–Gilbert inversion. The main lobe is smaller and the side lobes are removed. The line contours are in steps of 2 dB down from the maximum.

linearly related to the data

$$\hat{P}(\mathbf{p}_0) = \sum_{j=1}^K a_j(\mathbf{p}_0) d_j = \hat{\mathbf{a}}\mathbf{d}. \quad (\text{A5})$$

Due to the finite number of data, this estimate is a blurred image of the real spectrum. This can be written as

$$\hat{P}(\mathbf{p}_0) = \iint_{|\mathbf{p}| \leq p_{\max}} A(\mathbf{p}_0, \mathbf{p}) P(\mathbf{p}) d^2p \quad (\text{A6})$$

where  $A$  is the averaging kernel that blurs the real spectrum. For the conventional method,  $A$  is just the array response  $R$  given by (A3). Putting (A4) into (A5) and using (A6) we

find an expression for the averaging kernel  $A$

$$A(\mathbf{p}_0, \mathbf{p}) = \sum_{j=1}^K a_j(\mathbf{p}_0) G_j(\mathbf{p}) = \tilde{\mathbf{a}}(\mathbf{p}_0) \mathbf{G}(\mathbf{p}). \quad (\text{A7})$$

We now have to find those weights  $\mathbf{a}$  that give the optimum estimate  $\hat{P}$ . The most desirable kernel  $A$  would be a delta function, for then  $\hat{P}(\mathbf{p}_0)$  is closest to  $P(\mathbf{p}_0)$  in (A6). Therefore, we would want a kernel  $A$  that is as close to a delta function as possible; this kernel is found by minimizing

$$J = \iint_{|\mathbf{p}| \leq p_{\max}} [A(\mathbf{p}, \mathbf{p}_0) - \delta(\mathbf{p} - \mathbf{p}_0)]^2 d^2p + \varepsilon |\mathbf{a}|^2. \quad (\text{A8})$$

The second term in (A8) is added to assure stability of the inverse in the presence of errors. One can see the parameter  $\varepsilon$  as a trade-off between resolution (deltaness of the array response) versus variance (error in the result). The optimum value of  $\varepsilon$  can be estimated by calculating the variance and resolution as a function of  $\varepsilon$  and frequency; see Backus & Gilbert (1968) or chapter 12 of Aki & Richards (1980).

Minimizing (A8) with respect to the  $a_j$  and using (A7) gives the solution for the optimum weights

$$a_i(\mathbf{p}) = \sum_j (\mathbf{G}\tilde{\mathbf{G}} + \varepsilon \mathbf{I})_{ij}^{-1} G_j(\mathbf{p}). \quad (\text{A9})$$

The matrix  $\mathbf{G}\tilde{\mathbf{G}}$  is defined as

$$\begin{aligned} (\mathbf{G}\tilde{\mathbf{G}})_{ij} &= \iint_{|\mathbf{p}| \leq p_{\max}} G_i(\mathbf{p}) \tilde{G}_j(\mathbf{p}) d^2p \\ &= \iint_{|\mathbf{p}| \leq p_{\max}} e^{i\omega \mathbf{p} \cdot (\mathbf{r}_i - \mathbf{r}_j)} d^2p = \frac{2\pi p_{\max}}{\omega r_{ij}} J_1(\omega p_{\max} r_{ij}), \end{aligned} \quad (\text{A10})$$

where  $r_{ij}$  is the distance between stations  $i$  and  $j$ , and the integration is performed over the disc in  $\mathbf{p}$ -space with  $|\mathbf{p}| \leq p_{\max}$ . The expressions for  $A$  and  $\hat{P}$  now become

$$\mathbf{A}(\mathbf{p}_0, \mathbf{p}) = \tilde{\mathbf{G}}(\mathbf{p}_0) (\mathbf{G}\tilde{\mathbf{G}} + \varepsilon \mathbf{I})^{-1} \mathbf{G}(\mathbf{p}), \quad (\text{A11})$$

$$\hat{P}(\mathbf{p}_0) = \tilde{\mathbf{G}}(\mathbf{p}_0) (\mathbf{G}\tilde{\mathbf{G}} + \varepsilon \mathbf{I})^{-1} \mathbf{d}. \quad (\text{A12})$$

The array response for a vertically incident wave with frequency 0.05 Hz is shown in Fig. A1(b), for  $\varepsilon = 0$ . Working best at low frequencies, the Backus–Gilbert inversion has increased the resolution drastically. The main lobe is much smaller and side lobes are suppressed. At higher frequencies the side lobes are not removed totally from the spectrum, but as the position of these lobes is known, they can be removed from the spectrum with the CLEAN method (Högbom 1974).